Advanced Powder Technology 34 (2023) 104036

Contents lists available at ScienceDirect

Advanced Powder Technology

journal homepage: www.elsevier.com/locate/apt

Original Research Paper

Investigation of non-uniform characteristics in a 300 MW_{th} circulating fluidized bed with different coal feeding modes

Dali Kong [a], Shuai Wang [a,*], Jiahui Yu [a], Debo Li [c], Kun Luo [a,b,*], Jianren Fan [a,b]

[a] State Key Laboratory of Clean Energy Utilization, Zhejiang University, Hangzhou 310027, China
[b] Shanghai Institute for Advanced Study of Zhejiang University, Shanghai 200120, China
[c] Guangdong Diankeyuan Energy Technology Co., Ltd., Guangzhou 510080, Guangdong, China

ARTICLE INFO

Article history:
Received 25 September 2022
Received in revised form 31 March 2023
Accepted 4 April 2023
Available online 19 April 2023

Keywords:
Circulating fluidized bed
Coal combustion
Coal feeding mode
Numerical simulation
Gas pollutants

ABSTRACT

Circulating fluidized bed (CFB) has been practised in many engineering fields, but the non-uniform characteristics deteriorate combustion performance and system control. In this study, the improvement of external-loop and in-furnace non-uniformity of a 300 MW_{th} industrial-scale CFB with multiple cyclones by a dual-side coal feeding mode was numerically quantified. The results show that the pressure is non-uniformly distributed among three external loops, where the pressure in the middle loop seal is lower than that in the corner loop seals by 4.5 %. The pressure gradient positively correlates with the solid holdup. As compared with the traditional single-side coal feeding mode, the dual-side coal feeding mode: (i) promotes the final mixing degree by 11.15 %; (ii) extends the residence time of coal particles by 10.3 %; (iii) reduces the magnitude and fluctuation of the horizontal solid flux by 28.5 % and 77%, respectively; (iv) narrows the temperature range and reduces the mean temperature by 7 °C; (v) enhances the combustion of coal particles by consuming more O_2; (vi) decreases the concentrations of SO_2 and NO by 3 % and 5 %, respectively. The present study shows the superiority of the dual-side coal feeding mode to the traditional single-side coal feeding mode in the optimization of CFBs in practical industrial processes.

1. Introduction

Energy depletion and climate change call for the efficient utilization of fossil fuels. Among all utilization technologies, circulating fluidized bed (CFB) technology provides a promising route for the thermochemical conversion of fossil fuels, due to its advantages of high gas–solid contact efficiency, significant heat and mass transfer, wide fuel availability, and low gas pollutants. As shown in Fig. 1(a), a typical CFB system includes several parts such as a CFB boiler, reheater, heat exchanger, and screw feeder, in which the CFB boiler is composed of a furnace for coal combustion, a cyclone for gas–solid separation, and a loop seal for solid exchange. The CFB boiler is a dense gas–solid reacting system operating in the fast fluidization regime involving multi-scale structures (e.g., micro-scale inter-particle/phase interaction, mesoscale cluster/bubble evolution, reactor-scale internal circulation) and multi-physics processes (e.g., gas–solid mixing, heat transfer, drying, pyrolysis, combustion, and pollutant formation) (Fig. 1(b)). An in-depth understanding of the complex in-furnace phenomena is vital for the design, operation, and optimization of the CFB boiler. Many experimental efforts have been made to investigate the CFB in terms of the voidage distribution [1], dual-side refeed configuration [2], process control [3], ash formation characteristics, and N_2O emission [4]. However, harsh conditions and opaque nature make it difficult to unveil the multi-phase reacting flow inside the CFB through experiments. Besides, the trial-and-error strategies make the experiment expensive, unrepeated, and inefficient.

Numerical modelling provides a cost-effective, repeated, and efficient way to investigate the detailed in-furnace phenomena of the CFB. The existing numerical methods can be divided into Eulerian-Eulerian and Eulerian-Lagrangian frameworks. In the Eulerian-Eulerian framework, both gas and solid phases are assumed as continuous media, and the inter-particle collision is simplified by a kinetic theory of granular flow (KTGF) model, which is computationally efficient. As a mature method, the two-fluid model (TFM) under the Eulerian-Eulerian framework has been widely used in simulating chemical engineering processes [6], such as biomass gasification [7], chemical looping combustion [8], coal combustion [9], etc. However, the TFM approach has drawbacks in (i) complex closures of the solid phase; (ii) incapability of

* Corresponding authors at: State Key Laboratory of Clean Energy Utilization, Zhejiang University, Hangzhou 310027, China.
E-mail addresses: wshuai2014@zju.edu.cn (S. Wang), zjulk@zju.edu.cn (K. Luo).

https://doi.org/10.1016/j.apt.2023.104036
0921-8831/

Nomenclature

C_s	Specific heat capacity of particle (J/(kg·K))
C_V	Specific heat capacity of gas phase (J/(kg·K))
C	Model constant (-)
D_g	Mass diffusion coefficient of gas (m^2/s)
D_s	Drag function coefficient (-)
d_s	Particle diameter (m)
h_g	Specific enthalpy (J/kg)
f_s	Distribution function of particle (-)
$\boldsymbol{F}_{gs}$	Interphase force between the gas and particle phases (N)
$\boldsymbol{g}$	Gravitational acceleration (m/s^2)
ΔH_r	Heat source forming from chemical reactions (W/m^3)
m	Mass (kg)
$\delta \dot{m}_s$	Mass source term (kg/(m^3·s))
$\delta \dot{m}_{k,react}$	The net consumption or production rate of k^{th} gas species (kg/(m^3·s))
Nu	Nusselt number (-)
p_g	Pressure of gas phase (Pa)
P_s	Pressure constant (Pa)
Pr_t	Turbulent Prandtl number (-)
q	Heat flux (W/m^2)
$\dot{Q}_D$	Enthalpy diffusion term (W/m^3)
Re	Reynolds number (-)
S_{gs}, S_{gw}	Energy exchange term (W/m^3)
T	Temperature (K)
$\boldsymbol{u}$	Velocity(m/s)
$Y_{g,k}$	Mass fraction of gas specie k (-)

Greek symbols

θ	Volume fraction (-)
δ_{ij}	Unit tensor (-)
λ_{mol}	The molecular conductivity of the gas phase (W/(m·K))
λ_t	The turbulent conductivity of the gas phase (W/(m·K))
ρ	Density (kg/m^3)
τ_D	Particle collision damping time (s)
τ_g	Fluid stress tensor (Pa)
μ_t	Turbulent viscosity (kg/(m·s))
μ_l	Laminar viscosity (kg/(m·s))
μ	Shear viscosity (kg/(m·s))
τ_s	Inter-particle stress (Pa)
θ_{cs}	Particle volume fraction at close packing (-)
Δ	Sub-grid length scale (m)
B, α	Model constant (-)

Subscripts

g	Gas phase
s	Particle phase
i, j	Coordinate index

Acronyms

CFB	Circulating Fluidized Bed
CFD	Computational Fluid Dynamics
DEM	Discrete Element Method
MP-PIC	Multi-phase Particle-in-cell
PSD	Particle Size Distribution

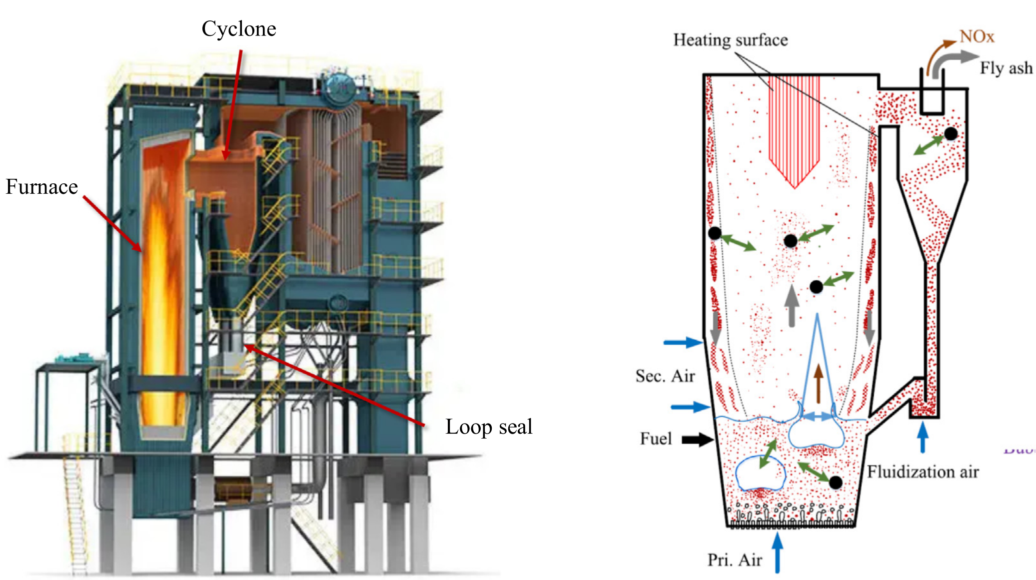

(a) (b)

Fig. 1. (a) Circulating fluidized bed (CFB) system; (b) flow characteristics in the CFB boiler [5].

obtaining particle-scale information. The Eulerian-Lagrangian framework overcomes the above issues by naturally tracking the trajectory of each particle, with the intrinsic capability of considering particle-scale properties (e.g., particle size distribution and particle shrinkage). As two typical approaches under the Eulerian-Lagrangian framework, the computational fluid dynamics-discrete element method (CFD-DEM) and multiphase particle-in-cell (MP-PIC) are the most used ones. In the former, the collision procedure between every two contacting particles is resolved by the DEM model using a tiny time-step, delivering a precise solution of dense gas–solid flow. The CFD-DEM approach has emerged to simulate multi-phase reacting flow in fluidized bed reactors [10], such as food grain drying [11], coal combustion [12], biomass gasification [13], chemical looping combustion [14], and solar panel waste recycling [15], to help understand the particle-scale mechanism of kinematic behaviours, heat transfer contribution, and particle shrinkage characteristics in lab-scale apparatuses within limited particle numbers ($\sim10^5$). However, it has been seldom applied to pilot- and industrial-scale fluidized bed reactors due to the intrinsic limitation of heavy computation cost. This issue is overcome by the MP-PIC approach, which combines the advantages of the TFM and CFD-DEM approach and achieves a trade-off between numerical accuracy and computational cost. Specifically, the MP-PIC approach adopts a parcel concept to lump a collection of original particles into a numerical parcel and simplifies the inter-particle collisions by introducing a solid stress model. In this way, the dense gas–solid system at a large scale can be analyzed through a reasonable number of computational particles, which makes the MP-PIC approach a great potential to model pilot- and industrial-scale CFBs.

So far, several studies have been conducted to explore coal combustion in CFBs under the single-side coal feeding mode by the MP-PIC approach. For example, Zeneli et al. [16] did a comprehensive discussion on the treatment of polydispersity of bed material that has been widely encountered in many industrial-scale CFB applications. The Eulerian-Eulerian method has no capacity of calculating particle-scale information, especially the particle size distribution (PSD), as the trajectory of each size group of particles needs to be handled by solving its transport equation. Such a treatment is impractical in simulating the industrial-scale apparatus with a significantly broad size distribution, which requires unaffordable computational memory. In contrast, the MP-PIC approach under the Eulerian-Lagrangian framework provides a novel measure for modelling polydisperse particulate flow, as it enables the explicit incorporation of the PSD in the numerical model, showing great potential in industrial-scale CFB applications. Kong et al. [17] studied the co-combustion characteristics of coal and refuse-derived fuel in a 0.5 MW_{th} CFB and demonstrated that the emissions of NOx, CO, SO_2, and HCl could be regulated by adjusting operating temperature and primary air ratio. Gu et al. [18] studied the oxy-fuel combustion in a 12 MW_{th} pilot-scale supercritical CO_2 (S-CO_2) CFB and found that increasing the inlet O_2 concentration increased the gas temperature, combustion efficiency, and desulfurization efficiency. Blaser and Corina [19] explored the optimization of flow fields in a 40 MW CFB. The results were validated against operational erosion experiments and used to redesign various components of the boiler. The optimized boiler has a 50 % reduction in erosion in the cyclone inlet region, a 47 % reduction in erosion in the suspension tube region, and a pressure drop 12 % lower than the original design. Xie et al. [20] investigated the co-combustion characteristics of municipal solid waste (MSW) and coal in an industrial-scale CFB. The results indicated that the emissions of NO and N_2O decreased while the SO_2 emission increased with the increasing coal mass share. The increase in the secondary air ratio could effectively reduce the NO_x emission, but there was no distinct tendency for the SO_2 emission. To summarize, the above-mentioned studies all focused on the single-side coal feeding mode. Previous studies have shown that the single-side coal feeding mode will lead to coal particles accumulating on the coal feeding side, resulting in poor particle mixing efficiency, uneven combustion, non-uniform temperature distribution, and hotspot formation in the furnace. Moreover, the uneven temperature and gas species distribution in the furnace will promote the formation of pollutants. For example, hot spots can lead to the formation of NO_x at high temperatures. On the coal feeding side, the lower oxygen concentration will promote the formation of CO. The dual-side coal feeding mode is expected to improve the above-mentioned defects caused by the single-side coal feeding mode. However, the optimization of the CFB with a dual-side coal feeding mode has not been reported. Besides, the previous studies only focused on the macroscopic hydrodynamics of lab-scale or subcritical CFB boilers, lacking an understanding of supercritical CFB boilers.

Accordingly, in this work, a three-dimensional (3-D) full-loop simulation of a 300 MW industrial-scale CFB boiler operating in a supercritical state is realized by a recently developed MP-PIC reactive model based on the Eulerian-Lagrangian framework. Compared with the low-capacity CFB boilers (10 $\sim$ 100 MW) operating in a subcritical state, it has the advantages of higher output power, lower coal consumption per unit power, and lower pollutant emission. Therefore, it is of great significance to carry out relevant research on the supercritical CFB boiler and its optimal design. The model integrates the gas–solid flow, heat transfer, and chemical reactions, successfully verified by comparing with the experimental data. The detailed gas-flow hydrodynamics and thermochemical characteristics hardly measured by experiment are simulated. Meanwhile, the improvement of flow uniformity and system performance using the dual-side coal feeding mode is quantified. The simulated results shed light on the design and operation of low-pollutant and high-efficiency power plants.

2. Methodology

In the MP-PIC approach, the gas phase is treated as a continuum and the gas turbulence is resolved by the large-eddy simulation (LES). For the solid phase, a parcel concept is used to lump several original particles into a numerical parcel, and a solid stress model is introduced to simplify the collision procedure. The particle dynamics is described by solving the transport equation of a particle distribution function (PDF). In this work, detailed reaction kinetics are implemented, including both heterogeneous and homogeneous reactions (e.g., pyrolysis, drying, char combustion, and pollutant removal reactions). The cut-cell technique was implemented to resolve the industrial-scale full-loop CFB with complex geometry structures. Based on the above improvements, the effects of different coal feeding modes on the particle-scale gas–solid motions and macro-scale reactor performance can be explored thoroughly, thereby further guiding reactor design and process optimization of practical CFB boilers. The mathematical model is detailed below.

2.1. Governing equations

The mass and momentum conservation equations for the gas phase are formulated as [21,22]:

$$\frac{\partial\left(\theta_g\rho_g\right)}{\partial t}+\nabla\cdot(\theta_g\rho_g\boldsymbol{u}_g)=\delta\dot{m}_s \tag{1}$$

$$\frac{\partial\left(\theta_g\rho_g\boldsymbol{u}_g\right)}{\partial t}+\nabla\cdot(\theta_g\rho_g\boldsymbol{u}_g\boldsymbol{u}_g)=-\nabla p_g+\rho_g\theta_g\boldsymbol{g}+\nabla\cdot(\theta_g\boldsymbol{\tau}_g)+\boldsymbol{F}_{gs} \tag{2}$$

where ρ_g is the density; $\boldsymbol{u}_g$ is the velocity vector; p_g is the pressure; θ_g is the volume fraction; $\boldsymbol{g}$ is the gravitational acceleration. $\boldsymbol{F}_{gs}$ is the inter-phase momentum exchange term. $\delta\dot{m}_s$ is the source term that links the reaction of the discrete phase and continuous phase, which is calculated by integrating the PDF, $f_s(\boldsymbol{x}_s, \boldsymbol{u}_s, m_s, T_s, t)$:

$$\delta\dot{m}_s=-\iiint f_s\frac{dm_s}{dt}dm_sd\boldsymbol{u}_sdT_s \tag{3}$$

where $\boldsymbol{x}_s$ is the spatial particle position; $\boldsymbol{u}_s$ is the particle velocity; m_s is the particle mass; T_s is the particle temperature. $\boldsymbol{\tau}_g$ is the stress tensor of the gas phase, given by:

$$\tau_{g,ij} = \mu\left(\frac{\partial u_i}{\partial x_j} + \frac{\partial u_j}{\partial x_i}\right) - \frac{2}{3}\mu\frac{\partial u_k}{\partial x_k}\delta_{ij} \tag{4}$$

$$\mu = \mu_l + \mu_t; \qquad \mu_t = C\rho_g\Delta^2 \times \sqrt{\left(\frac{\partial u_i}{\partial x_j} + \frac{\partial u_j}{\partial x_i}\right)^2}; \qquad \Delta = \sqrt[3]{\Delta x\Delta y\Delta z} \tag{5}$$

where μ_l is the laminar viscosity and μ_t is the turbulent viscosity. The latter is evaluated by a Smagorinsky model under the LES framework [23].

The energy and species conservation equations of the gas phase are given by:

$$\frac{\partial(\theta_g\rho_g h_g)}{\partial t} + \nabla\cdot(\theta_g\rho_g\boldsymbol{u}_g h_g) = \theta_g\left(\frac{\partial p_g}{\partial t} + \boldsymbol{u}_g\cdot\nabla p_g\right) - \nabla\cdot(\theta_g q) + \dot{Q}_D + S_{gs} + S_{gw} - \Delta H_{rg} \tag{6}$$

$$\frac{\partial(\theta_g\rho_g Y_{g,k})}{\partial t} + \nabla\cdot(\theta_g\rho_g\boldsymbol{u}_g Y_{g,k}) = \nabla\cdot(\theta_g\rho_g D_{g,k}\nabla Y_{g,k}) + \delta\dot{m}_{k,react} \tag{7}$$

where h_g and $Y_{g,k}$ are the enthalpy of the gas mixture and the mass fraction of k^{th} gas species, respectively. $\delta\dot{m}_{k,react}$ is the consumption or production of k^{th} gas species. $D_{g,k}$ denotes the mass diffusion coefficient. q is the heat flux, related to the molecular thermal conductivity and turbulence thermal conductivity of the gas phase:

$$q = (\lambda_{mol} + \lambda_t)\nabla T_g \tag{8}$$

$$\lambda_t = \frac{C_s\mu_t}{\mathrm{Pr}_t} \tag{9}$$

where C_s and Pr_t represent the specific heat capacity and turbulent Prandtl number of the gas phase, respectively. ΔH_{rg} is the heat of reaction. S_{gs} and S_{gw} are the source terms of gas-particle and gas-wall heat transfer, which are written as:

$$S_{gs} = \iiint f_s\left\{m_s\left[D_s(\boldsymbol{u}_g - \boldsymbol{u}_s)^2 - C_V\frac{dT_s}{dt}\right] - \frac{dm_s}{dt}\left[h_s + \frac{1}{2}(\boldsymbol{u}_g - \boldsymbol{u}_s)^2\right]\right\}dm_s d\boldsymbol{u}_s dT_s \tag{10}$$

$$S_{gw} = h_{gw}A_{gw}(T_w - T_g) \tag{11}$$

where C_V is the specific heat capacity of the particle. The convective heat transfer coefficient h_{gw} is calculated by the correlation:

$$h_{gw} = \mathrm{Nu_w}\lambda_g/\mathrm{d_s} \tag{12}$$

$$\mathrm{Nu_w} = 0.023\mathrm{Re}^{0.8}\mathrm{Pr}^{\mathrm{n}} \tag{13}$$

where n and d_h stand for the model constant and the hydraulic diameter, respectively.

The enthalpy h_s and enthalpy diffusion $\dot{Q}_D$ of the gas phase are formulated as:

$$h_g = \sum_{k=1}^{N_k} h_{g,k}Y_{g,k} = \sum_{k=1}^{N_k} Y_{g,k}\left(\int_{T_0}^{T_g} C_{s,k}dT + \Delta h_{g,k}\right) \tag{14}$$

$$\dot{Q}_D = \sum_{k=1}^{N_k}\nabla\cdot\left(h_k\theta_g\rho_g D_g\nabla Y_{g,k}\right) \tag{15}$$

where T_0 and T_g are the reference temperature and operating temperature, respectively. $h_{g,k}$ is the enthalpy of k^{th} gas species and N_k is the total number of gas species. D_g is the mass diffusivity of the gas phase.

For the solid phase, the PDF $f_s(x_s, \boldsymbol{u}_s, m_s, T_s, t)$ is adopted to describe the particle dynamics by solving its transport equation as:

$$\frac{\partial f_s}{\partial t} + \nabla\cdot(f_s\boldsymbol{u}_s) + \nabla\boldsymbol{u}_s\cdot(f_s\boldsymbol{A}) = \frac{f_D - f_s}{\tau_D} \tag{16}$$

$$\mathbf{A} = \frac{d\boldsymbol{u}_s}{dt} = D_s(\boldsymbol{u}_g - \boldsymbol{u}_s) - \frac{1}{\rho_s}\nabla p_g - \frac{1}{\theta_s\rho_s}\nabla\tau_s + \boldsymbol{g} + \frac{\bar{\boldsymbol{u}}_s - \boldsymbol{u}_s}{2\tau_D} \tag{17}$$

where τ_D and $\boldsymbol{A}$ are the particle damping time and particle acceleration, respectively. O'Rourke et al. [24] originally proposed a preliminary correlation for calculating the collision damping time that is based on equilibrium kinetic theory, in which the collision damping time τ_D is a function of spatial location and time. They further modified the model to calculate collision damping time by considering the effects of particle restitution and the non-equilibrium distributions of particle properties. The modified correlation is applicable for modelling polydisperse particle flows with non-equilibrium velocity distributions, and has been widely applied to the simulation of reactive gas–solid flow in fluidized bed reactors [25,26,27]. Therefore, the correlation for τ_D developed by O'Rourke et al. [22] is adopted in this work. $\bar{\boldsymbol{u}}_s$ represents the mass-averaged solid velocity. Particle normal stress τ_s can be calculated as [28]:

$$\tau_s = \frac{P_s\theta_s^\beta}{\max[(\theta_{cs} - \theta_s), \alpha(1 - \theta_s)]} \tag{18}$$

$$\theta_s = \iiint f_s\frac{m_s}{\rho_s}dm_s d\boldsymbol{u}_s dT_s \tag{19}$$

where θ_s (=1-θ_g) is the solid volume fraction. P_s, α, and β are model constants. θ_{cs} is the solid volume fraction at the close-packing state.

The inter-phase momentum exchange term $\boldsymbol{F}_{gs}$ is evaluated as:

$$\boldsymbol{F}_{gs} = -\iiint f_s\left\{m_s\left[D_s(\boldsymbol{u}_g - \boldsymbol{u}_s) - \frac{\nabla p_g}{\rho_s}\right] + \boldsymbol{u}_s\frac{dm_s}{dt}\right\}dm_s d\boldsymbol{u}_s dT_s \tag{20}$$

where D_s is the drag function coefficient related to solid concentration, particle Reynolds number, and slip velocity. The selection of the drag model plays a vital role in reasonably predicting gas–solid flow characteristics. Due to the co-existence of bed material and coal particles with different size distributions, a drag model considering the polydispersity effect is employed in this work [29,30]:

$$D_s = \frac{18\mu_g\theta_g(1 - \theta_g)}{d_{s,i}^2}F_i \tag{21}$$

$$F_i = (\theta_g y_i + (1 - \theta_g)y_i^2 + 0.064\theta_g y_i^3)F \tag{22}$$

$$F = \frac{10(1 - \theta_g)}{\theta_g^2} + \theta_g^2\left(1 + 1.5(1 - \theta_g)^{0.5}\right) + \frac{0.413Re_s}{24\theta_g^2}\left[\frac{\theta_g^{-1} + 3\theta_g(1 - \theta_g) + 8.4Re_s^{-0.343}}{1 + 10^{3(1-\theta_g)}Re_s^{-0.5-2(1-\theta_g)}}\right] \tag{23}$$

$$y_i = \frac{d_{s,i}}{d_s} \tag{24}$$

$$d_s = \frac{\sum_{i=1}^{c}N_i d_{s,i}^3}{\sum_{i=1}^{c}N_i d_{s,i}^2} \tag{25}$$

$$\mathrm{Re}_s = \frac{\rho_g\varepsilon_g|\boldsymbol{u}_g - \boldsymbol{u}_s|\mathrm{d_s}}{\mu_g} \tag{26}$$

where c is the total number of particles in the system, $d_{p,i}$ is the diameter of particle i, N_i is the number of particles with the same size as particle i.

Table 1
Chemical reactions during the CFB combustion.

No.	Chemical reactions
R1	Drying process: Moisture → H_2O $_{(g)}$
R2	Pyrolysis process:Coal → Char ($CN_{0.014}S_{0.004}$) + CH_4 + H_2 + CO_2 + CO + H_2O + NH_3 + HCN + H_2S + Tar ($C_{10.77}H_{14.63}O_{0.22}$) + Ash
R3	CO + $0.5O_2$ → CO_2
R4	H_2 + $0.5O_2$ → H_2O
R5	CH_4 + $2O_2$ → CO_2 + $2H_2O$
R6	Tar ($C_{10.77}H_{14.63}O_{0.22}$) + 14.31750_2 → $10.77CO_2$ + 7·.$315H_2O$
R7	HCN + $0.75O_2$ → CNO + 0·.$5H_2O$
R8	CNO + $0.5O_2$ → NO + CO
R9	CNO + NO → N_2O + CO
R10	N_2O + CO → N_2 + CO_2
R11	N_2O + $0.5O_2$ → N_2 + O_2
R12	NH_3 + $1.25O_2$ → NO + 1·.$5H_2O$
R13	NH_3 + $0.75O_2$ → 0.5 N_2 + 1·.$5H_2O$
R14	NO + NH_3 + $0.25O_2$ → N_2 + 1·.$5H_2O$
R15	NO + CO → 0.5 N_2 + CO_2
R16	H_2S + $1.5O_2$ → SO_2 + H_2O
R17	$CN_{0.014}S_{0.004}$ + $1.022CO_2$ → $0.004SO_2$ + 2.022CO + 0.014NO
R18	$CN_{0.014}S_{0.004}$ + 1·.$022H_2O$ → $0.004SO_2$ + CO + 0.014NO + $1.022H_2$
R19	$CN_{0.014}S_{0.004}$ + $1.011O_2$ → $0.004SO_2$ + CO_2 + 0.014NO
R20	$CN_{0.014}S_{0.004}$ + 1.008NO → $0.004SO_2$ + CO + 0.511 N_2
R21	$CN_{0.014}S_{0.004}$ + $1.008N_2O$ → $0.004SO_2$ + CO + 1.011 N_2

The mass and energy conservation equations based on each parcel are given by:

$$\frac{dm_s}{dt} = \sum_{i=1}^{N} \frac{dm_{s,i}}{dt} \tag{27}$$

$$m_s C_V \frac{dT_s}{dt} = Q_{sg} + Q_{radi} - \Delta H_{rs} \tag{28}$$

where Q_{sg} and Q_{radi} represent the convective heat transfer flux and radiative heat transfer flux, respectively. They can be evaluated as:

$$Q_{sg} = \frac{\lambda_g \mathrm{Nu}_s}{d_s} A_s (T_g - T_s) \tag{29}$$

$$Q_{radi} = \sigma \varepsilon_s A_s \left(T_{b,local}^4 - T_s^4\right) \tag{30}$$

where A_s is the particle surface; σ and ε_s are the Stefan-Boltzmann constant and particle emissivity, respectively. $T_{b,local}$ and Nu_s are the local environment temperature and particle Nusselt number, respectively.

2.2. Reaction kinetics

Drying, pyrolysis, homogeneous combustion, heterogeneous combustion, and pollutants formation are considered in modelling the coal combustion process. The coal particle is initially composed of moisture, volatile, char, and ash, among which the volatile consists of Tar, CH_4, CO, CO_2, H_2, H_2O, NH_3, HCN and H_2S. The proportion of each component can be calculated by the related correlations [31]. The molecular formula of tar and char are determined as $C_{10.77}H_{14.63}O_{0.22}$ and $CN_{0.014}S_{0.004}$. The main reactions and the corresponding kinetic parameters in the simulation are listed in Table 1 and Table 2 [20,21,31,32,33,34]. During the chemical reactions, the particle diameter changes due to the mass loss of fuel particles [35,36].

3. Numerical settings

3.1. Model setup

In this study, the investigated object is a 300 MW_{th} industrial-scale CFB boiler installed in Guangdong Province, China. The CFB consists of one furnace and three external circulation systems. As shown in Fig. 2 (a), the width, height, and depth of the furnace are 8.96 m, 39.7 m, and 28 m, respectively. The primary air with a volumetric flow rate of 474100 m^3/h is introduced into the furnace from the bottom distributor at 270 ℃ while the secondary air with a volumetric flow rate of 333200 m^3/h is injected from the lower part of the furnace at 340 ℃. The coal particles with a mass flow rate of 44.75 kg/s are fed from the lower part of the furnace. The coal material particles and bed material particles (i.e.,

Table 2
Reaction kinetic parameters.

No.	Reaction rate r_i	Reaction rate coefficient K_i
R1	$r_1 = K_1 C_{moisture}$ (kmol·m^{-3}s^{-1})	$K_1 = 1.1 \times 10^5 \exp(-1.07 \times 10^4/T)$
R2	$r_2 = K_2 C_{valotile}$ (kmol·m^{-3}s^{-1})	$K_2 = 2.07 \times 10^4 \exp(-8780/T)$
R3	$r_3 = K_3\ C_{CO} C_{H_2O}^{0.5} C_{O_2}^{0.25} C_{CO_2}^{-0.32}$ (kmol·m^{-3}s^{-1})	$K_3 = 5.56 \times 10^7 \exp(-15145/T)$
R4	$r_4 = K_4\ C_{H_2} C_{O_2}^{0.5}$ (kmol·m^{-3}s^{-1})	$K_4 = 5.69 \times 10^{11} \exp(-1.465 \times 10^8/RT)$
R5	$r_5 = K_5\ C_{CH_4} C_{O_2}$ (kmol·m^{-3}s^{-1})	$K_5 = 3.552 \times 10^{14} T^{-1} \exp(-15.7/T)$
R6	$r_6 = K_6\ C_{Tar} C_{O_2}$ (kmol·m^{-3}s^{-1})	$K_6 = 3.8 \times 10^7 \exp(-6680/T)$
R7	$r_7 = K_7\ C_{HCN} C_{O_2}$ (kmol·m^{-3}s^{-1})	$K_7 = 2.14 \times 10^8 \exp(-10000/T)$
R8	$r_8 = K_8\ C_{CNO} C_{O_2} \frac{k_a C_{NO}}{K_a + k_b C_{NO}}$ (kmol·m^{-3}s^{-1})	$K_8 = K_9 = 2.14 \times 10^8 \exp(-10000/T)$
R9	$r_9 = K_9\ C_{CNO} C_{O_2} \frac{k_a C_{NO}}{K_a + k_b C_{NO}}$ (kmol·m^{-3}s^{-1})	$k_b / k_a = 1.02 \times 10^{12} \exp(-25499/T)$
R10	$r_{10} = K_{10}\ C_{N_2O} C_{CO}$ (kmol·m^{-3}s^{-1})	$K_{10} = 2.51 \times 10^{11} \exp(-23180/T)$
R11	$r_{11} = K_{11}\ C_{N_2O}$ (kmol·m^{-3}s^{-1})	$K_{11} = 1.75 \times 10^8 \exp(-23800/T)$
R12	$r_{12} = K_{12}\ C_{NH_3} C_{O_2}$ (kmol·m^{-3}s^{-1})	$K_{12} = 2.73 \times 10^{17} \exp(-38160/T)$
R13	$r_{13} = K_{13}\ C_{NH_3} C_{O_2}$ (kmol·m^{-3}s^{-1})	$K_{13} = 5.07 \times 10^{14} \exp(-35200/T)$
R14	$r_{14} = K_{14}\ C_{NH_3}^{0.5} C_{O_2}^{0.5} C_{NO}^{0.5}$ (kmol·m^{-3}s^{-1})	$K_{14} = 3.38 \times 10^{13} \exp(-29400/T)$
R15	$r_{15} = K_{15} \frac{K_{15a} C_{NO} (K_{15b} C_{CO} + K_{15c})}{K_{15a} C_{NO} + K_{15b} C_{NO} + K_{15c}}$ (mol·m^{-3}s^{-1})	$K_{15} = 1.952 \times 10^7 \exp(-19000/T)$ $K_{15a} = 18.26$, $K_{15b} = 7.86$, $K_{15c} = 0.002531$
R16	$r_{16} = K_{16}\ C_{H_2S} C_{O_2}$ (kmol·m^{-3}s^{-1})	$K_{16} = 2.12 \times 10^{11} T\exp(-24500/T)$
R17	$r_{17} = K_{17f}\ C_{CO_2}$ - $K_{17r}\ C_{CO}^2$ (mol·m^{-3}s^{-1})	$K_{17f} = 1.272 m_s T\exp(-1.88 \times 10^8/RT)$ $K_{17r} = 1.044 \times 10^{-4} m_s T^2 \exp(-5.256 \times 10^7/RT–20.92)$
R18	$r_{18} = K_{18f}\ C_{H_2O}$- $K_{18r}\ C_{H_2} C_{CO}$ (mol·m^{-3}s^{-1})	$K_{18f} = 1.272 m_s T\exp(-1.88 \times 10^8/RT)$ $K_{18r} = 1.044 \times 10^{-4} m_s T^2 \exp(-1.96 \times 10^7/RT - 17.29)$
R19	$r_{19} = K_{19}\ C_{O_2}$ (kmol·m^{-3}s^{-1})	$K_{19} = 4.34 \times 10^7 \varepsilon_s T\exp(-1.13 \times 10^8/RT)$
R20	$r_{20} = \frac{6\varepsilon_s \rho_s Y_c}{d_s \rho_c} K_{20}\ C_{NO}$ (kmol·m^{-3}s^{-1})	$K_{20} = 5.85 \times 10^7 \exp(-12000/\ T)$
R21	$r_{21} = \frac{6\varepsilon_s \rho_s Y_c}{d_s \rho_c} K_{21}\ C_{N_2O}$ (kmol·m^{-3}s^{-1})	$K_{21} = 1.74 \times 10^{10} \exp(-16983/\ T)$

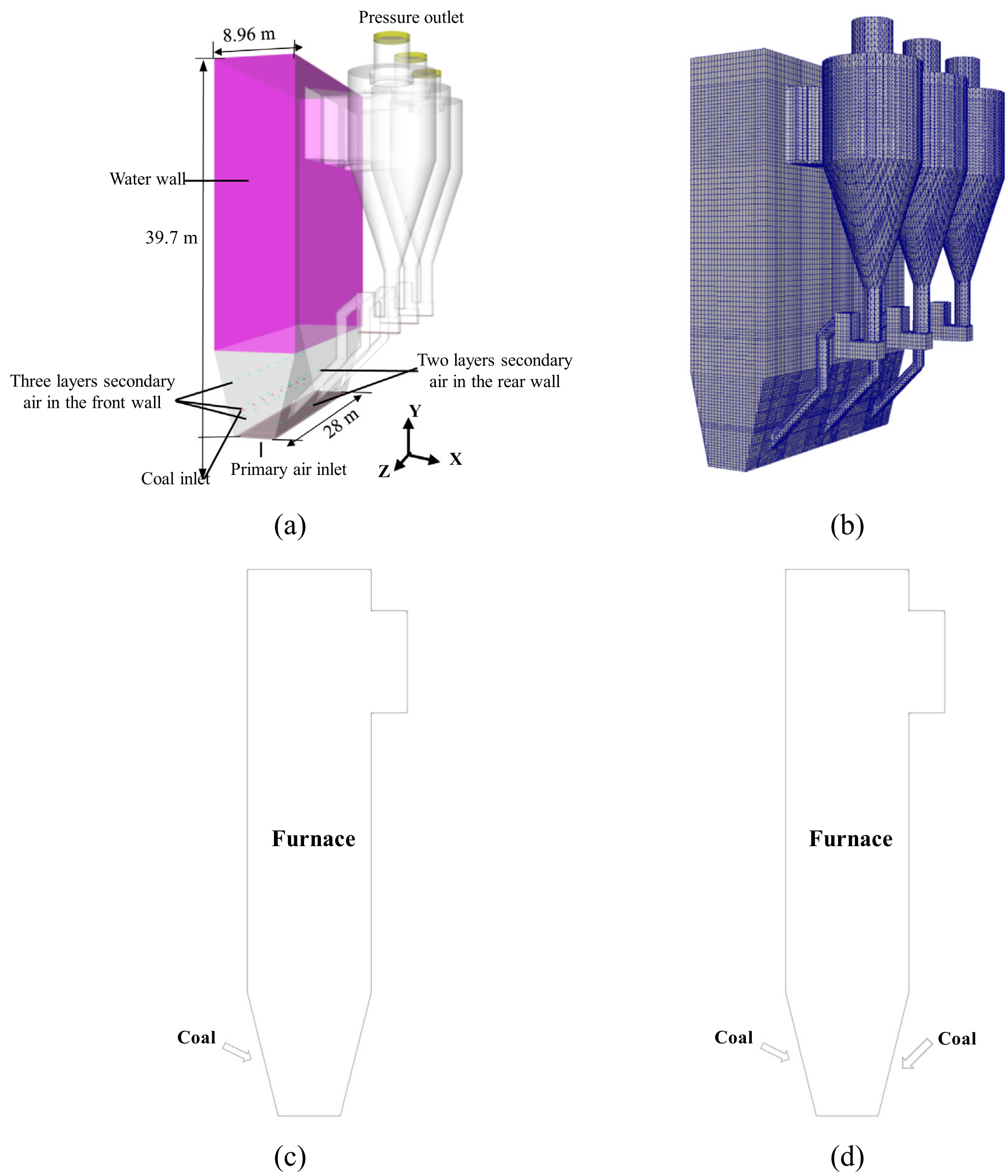

Fig. 2. The investigated 300 MW_{th} CFB: (a) Geometry configuration; (b) computational grids; (c).single-side coal feeding mode; (d) dual-side coal feeding mode.

sand) have a density of 1300 kg/m^3 and 2600 kg/m^3, respectively. The excessive air ratio is 1.3. The diameter of the coal particles follows a distribution, as listed in Table S1 of the Supporting Information. Besides, the proximate analysis and ultimate analysis of the coal particles are listed in Table S2 of the Supporting Information. Sand particles follow the size distribution as shown in Fig. S1 of the Supporting Information, with a Sauter mean diameter of 300 μm. The detailed gas–solid properties and operating conditions are listed in Table 3. As shown in Fig. 2 (b), the computational domain is divided into structured grids by an advanced cut-cell technique, and some grids with an over-small size are removed or merged to optimize grid quality. Moreover, some regions (e.g., the components junctions and cyclone separator) are refined to accurately capture the geometry configuration.

Before the simulation, the boundary condition should be set properly. In this work, the boundary conditions are determined based on the data measured from the real CFB boiler [37], considering the non-uniform distribution of gas–solid flow in three cyclone separators as demonstrated in previous literature

Table 3
Operating parameters in the simulation.

Parameters		Value
Primary air inlet (m^3/h)		474,100
Secondary air inlet (m^3/h)		333,200
Coal feeding rate (kg/s)		44.75
The temperature of primary air (°C)		270
The temperature of secondary air (°C)		340
Gauge pressure at cyclone outlet (kPa)	#1	−1.55
	#2	−1.77
	#3	−1.52
Particle density (kg/m^3)	Coal material	1300
	Bed material	2600
Initial bed temperature (°C)		880
Water wall temperature (°C)		340
Excess air ratio (-)		1.3
Solid volume fraction at close pack (-)		0.58
particle normal-to-wall retention coefficient (-)		0.99
particle tangential-to-wall retention coefficient (-)		0.3
Fraction coefficient (-)		0.3

[38,39]. Specifically, the primary and secondary air inlets are assigned as velocity inlet boundary conditions while the three cyclone outlets are specified as pressure outlet boundary conditions with Gauge pressure of −1.55 kPa, −1.77 kPa, and −1.52 kPa, respectively. The wall of the dilute region (Y > 9 m) of the furnace is covered by a water wall, which is set as an isothermal wall boundary condition with a constant temperature of 340 ℃. The dense region (Y < 9 m) of the furnace and the cyclone separators are assigned as adiabatic wall boundary conditions. Initially, the sand particles are packed in the bottom of the furnace and loop seals. The single-side and dual-side coal feeding modes are shown in Fig. 2 (c) and (d). The injection position with the dual-side coal feeding mode is symmetrically arranged with respect to the central plane. The case with the single-side coal feeding mode is employed as the base case, compared with the dual-side coal feeding mode using the same coal feeding rate. Each case was performed with a total physical time of 100 s.

3.2. Grid-independence test

Three sets of computational grids, i.e., 0.5 million (coarse grid), 0.85 million (medium grid), and 1.25 million (fine grid) are employed in this study to determine the optimal grid size for the simulation. As shown in Fig. 3, the profiles of solid mass flow rate and gas species first evolve and then fluctuate around fixed values after the system achieves an equilibrium state at t = 40 s. Thus, it is reasonable to obtain the time-averaged data by averaging the corresponding variables during the last 60 s. Moreover, the time-averaged solid mass flow rate under three grid resolutions are 1603 kg/s, 1539 kg/s, and 1612 kg/s, respectively. A significant discrepancy can be observed between the coarse grid and the other two grids. Refining the computational grid from the medium resolution to the fine resolution insignificantly influences the results. To balance computational costs and numerical accuracy, the medium grid is used in the following simulations.

4. Results and discussion

4.1. Model validation

In this section, the MP-PIC reactive model is validated against the experimental data in terms of solid circulation rate, pressure distribution, temperature distribution, and gas species to demonstrate the reasonability of the integrated model in predicting flow hydrodynamics, heat transfer, and chemical reactions. The time-averaged numerical results are used to compare with the experimental data. In this work, the time-averaged operation is conducted after the hydrodynamics and thermochemical behaviours reach a dynamic steady state in the system. The time-averaged operation and its standard deviation (also error lines of data in this work) of a quantity (ξ) are given by:

$$\xi_{ave} = \frac{1}{n}\sum_{j=1}^{n}\xi_j \tag{31}$$

$$\xi_{std} = \sqrt{\frac{1}{n}\sum_{j=1}^{n}\left(\xi_{ave}-\xi_j\right)^2} \tag{32}$$

where ξ_j is the instantaneous value of the quantity. ξ_{ave} is the time-averaged value of the quantity. ξ_{std} is the standard deviation of the time-averaged operation. n is the sampling number of the output data. For example, if the data are saved for every 0.01 s, n has a value of 6000 during the period of 40–100 s.

4.1.1. Validation I: 300 MW_{th} industrial-scale CFB

The MP-PIC reactive model is first validated with hydrodynamics and thermal characteristics in a 300 MW_{th} industrial-scale CFB. Three monitoring planes are specified in the loop seal to gain the solid mass flow rate. The material circulation ratio (MCR) is defined as the ratio of the total solid mass flow rate to the fuel feeding rate. After the system achieves the steady state, the time-averaged solid mass flow rates at the three monitoring planes are 538 kg/s, 470 kg/s, and 531 kg/s, respectively. The differences are attributed to the non-uniform gas–solid distribution among three cyclones as demonstrated in our previous work [38]. Combining the coal feeding rate of 44.75 kg/s, the MCR obtained from the simulation is 34.4, which is in line with the designed value of 30 [37]. The slight discrepancy is acceptable for such an industrial-scale apparatus.

The temperature field in the CFB can comprehensively reflect the heat and mass transfer and thermochemical characteristics in the furnace. The time-averaged temperature distribution along with the horizontal line at the height of 12.1 m predicted by the current model is further compared with the experiment data. As shown in Fig. 4, the temperature in the furnace is about 920 ∼ 950 °C, and the temperature in the near-wall region is lower because of the heat absorption of the water wall. The predicted profile well captures the distribution characteristics of “high temperature in the middle region and low temperature in the near-wall region”. Moreover, the relative error between the predicted values and experimental data is smaller than 4%, which is acceptable in practical industrial processes.

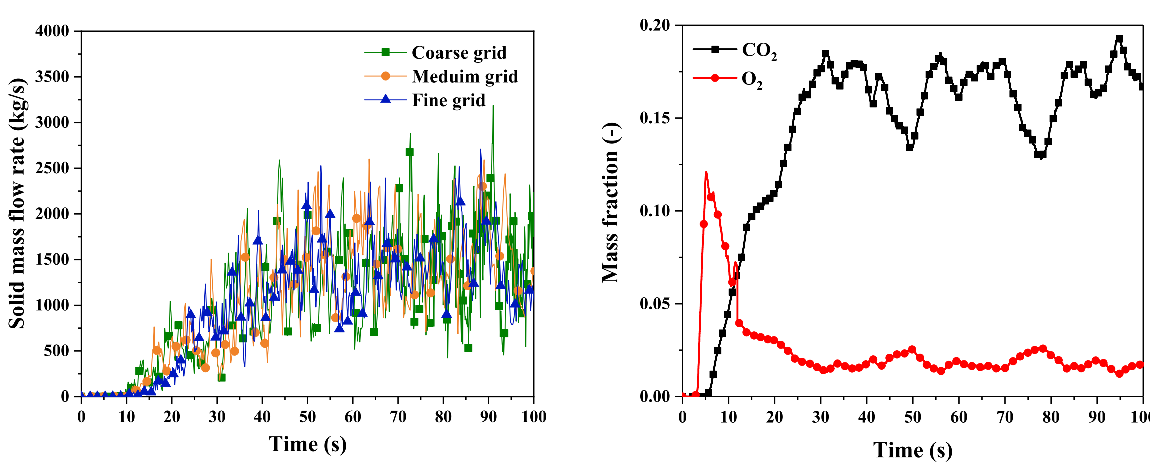

(a)   (b)

Fig. 3. (a) Time-evolution profiles of solid mass flow rate under different grid resolutions; (b) time-evolution of gas species at the cyclone outlet.

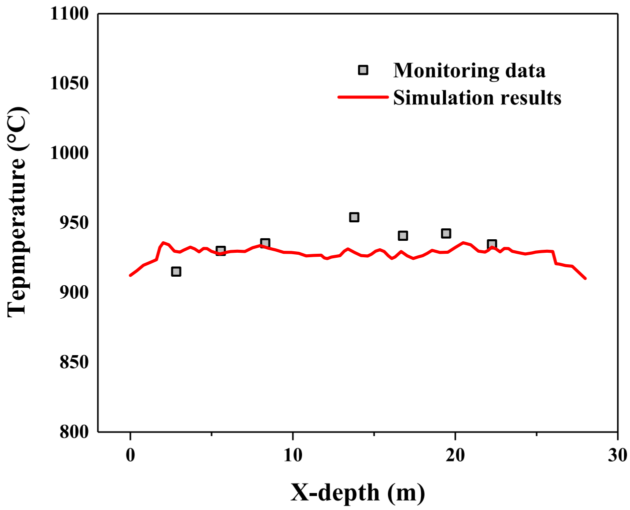

Fig. 4. Comparison of the horizontal temperature distribution between the current simulation results and experimental data.

4.1.2. Validation II: 0.5 MW$_{th}$ pilot-scale CFB

The MP-PIC reactive model is further validated with thermochemical characteristics in a 0.5 MW$_{th}$ pilot-scale CFB installed at Zhejiang University, China. The coal and refuse-derived fuel (RDF) are co-combusted in the furnace, which has a height of 11.2 m and a cross-section area of 330 × 330 mm^2 for the dilute part. The coal and RDF feeding inlets are located at the height of 3.0 m and 5.0 m of the furnace, respectively. The ratio of primary air to secondary air is maintained at 7:3, and the total mass flow rate of coal and RDF is 0.1736 kg/s. The detailed gas–solid parameters and operating conditions can refer to our previous publication [17]. As shown in Fig. 5, the model satisfactorily captures the temperature distribution in the furnace, and the relative error is less than 8%. In addition, the predicted concentration of gas species at the outlet agrees well with the experimental data.

To summarize, the present MP-PIC reactive model is reasonable to be used to simulate dense gas–solid reacting flow regarding hydrodynamics, heat transfer, and chemical reactions in the CFBs.

4.2. Flow hydrodynamics

Gas-solid flow hydrodynamics significantly affects the thermochemical characteristics and overall performance of the CFB. Fig. 6 shows the instantaneous in-furnace hydrodynamics of the 300 MW$_{th}$ CFB under the single-side coal feeding mode at t = 60 s. The dense phase is observed in the lower part of the bed, where the high particle concentration, violent particle interactions, and significant heat and mass transfer interconnect. The solid holdup decreases along with the bed height due to the interphase momentum exchange. Particles inside the furnace are fluidized by the introduced gas flow, and then the gas–solid flow is separated in the cyclone, finally, the particles are transported into the furnace through the loop seal. After being fed into the furnace, coal particles rapidly release moisture and volatile matter in a short period [41,42], with only carbon residual left. The carbon conversion reaction often takes hundreds of seconds to complete [43,44,45], and thus many coal particles consisting of carbon may reside in the loop seal due to the density-induced segregation [46], which can be evidenced by the spatial distribution of particle radius. Vigorous vertical particle velocity (Usy) is observed in the furnace, due to the dominant role of the vertically introduced gas flow from the bottom distributor. Besides, high vertical velocities of particles appear in the inclined part of the loop seal, which guarantees the transportation of particles into the furnace to achieve full-loop recirculation. Horizontal migration of particles (Usx, Usz) is also observed in the furnace, which results from the combined effect of interparticle/phase interactions, cluster formation/evolution, and coal feeding/particle recycling. The swirling flow in the cyclone can be characterized by horizontal particle velocities. The unique feature of gas–solid flow with "spinning downwards near the wall and moving upwards in the core" ensures the high separation efficiency of particles in the cyclone [47,48].

To quantitatively describe the gas–solid flow state in the bed, the time-averaged solid holdup and particle axial velocity distributions along the X direction under different coal feeding modes on the central slice in the depth direction (Z = 14 m) are extracted, the results are shown in Fig. 7. With the two coal feeding modes, the horizontal distribution of solid holdup at the bottom of the CFB shows strong heterogeneity, and the solid holdup near the wall on the right side is much higher than that on the left side, which is caused by the unique structure of the single-side coal feeding mode. In contrast, due to the introduction of coal particles from the right side, the dual-side coal feeding mode promotes the radial uneven distribution of solid holdup at the bottom of the CFB. With the increase in height, the solid holdup decreases significantly. In the single-sided coal feeding mode, the particles on the left side move upwards and the particles on the right side move downwards at all heights. However, the non-uniformity of the radial

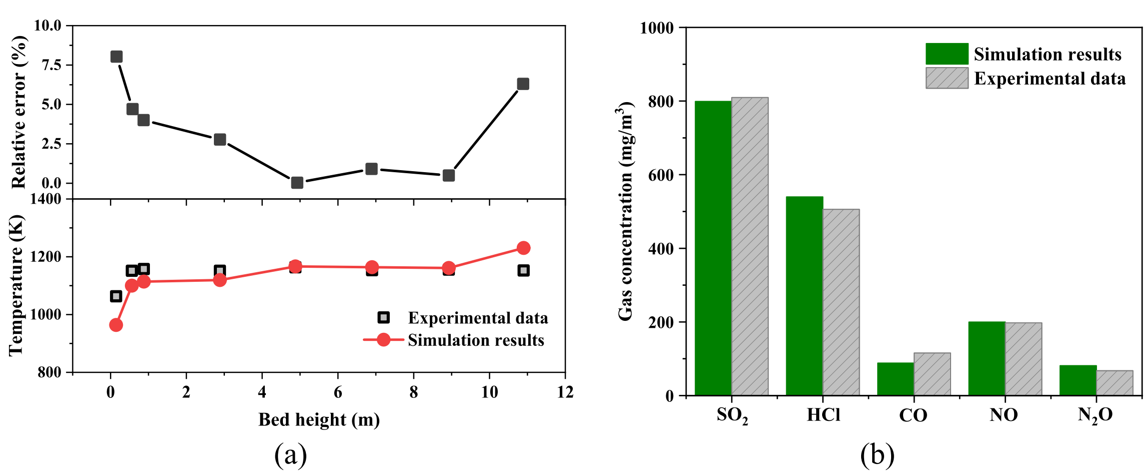

Fig. 5. Comparisons of the predicted temperature distribution (a) and gas species (b) with the experimental data [40], T$_b$ = 880 °C.

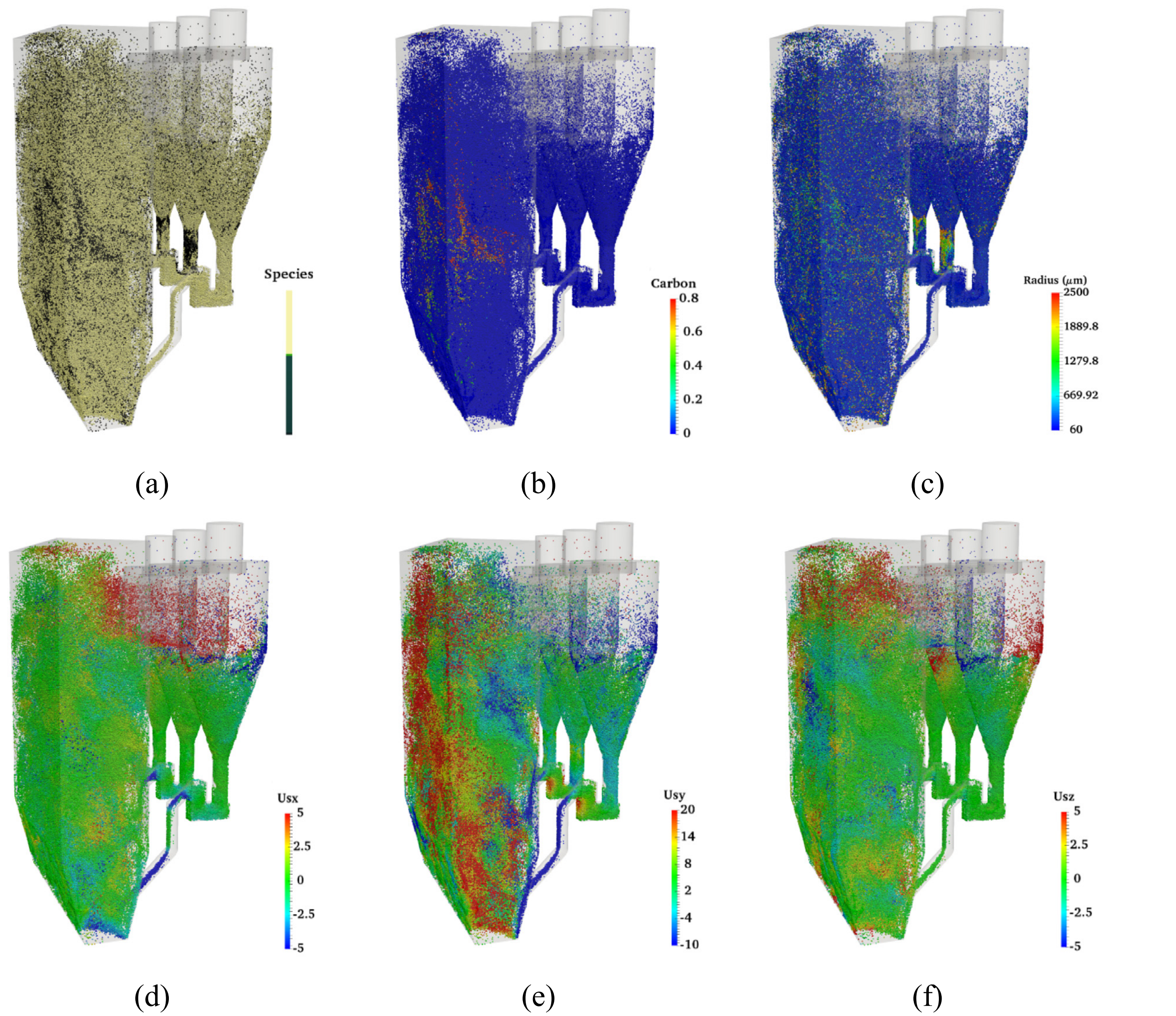

Fig. 6. Snapshots of particle information in the full-loop CFB: (a) solid species; (b) carbon composition; (c) particle radius; (d) Usx; (e) Usz; (f) Usy. Note that the particle size is enlarged for better visualization.

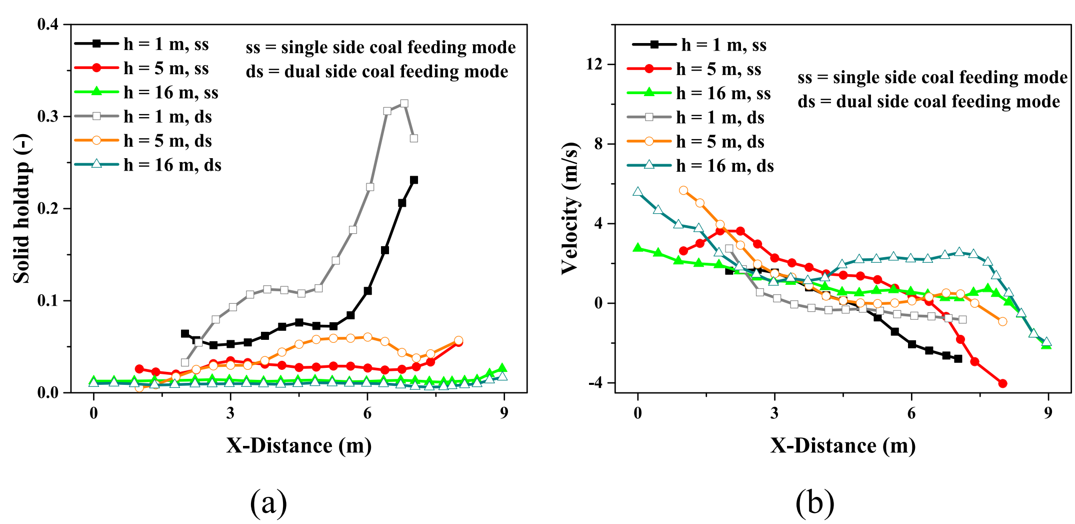

Fig. 7. Solid holdup and particle axial velocity distributions along the X direction under different coal feeding modes.

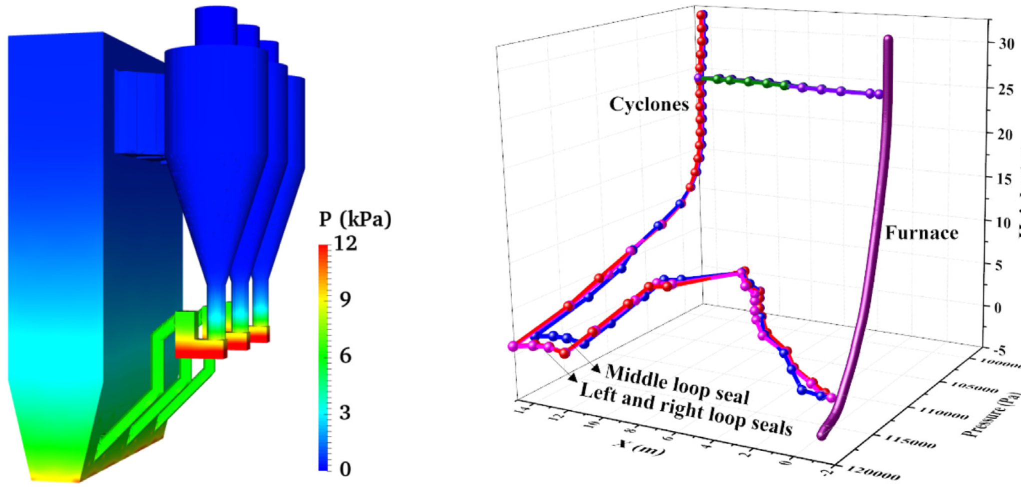

(a) (b)

Fig. 8. (a) Pressure distribution of the whole CFB; (b) pressure balance in the three loops.

distribution of particle velocity is weakened in the dual-side coal feeding mode, and the particle backflow near the right wall is inhibited.

Fig. 8 gives the full-loop distribution of the time-averaged pressure in the CFB after the system reaches the equilibrium state. Large pressure and pressure gradient are observed at the bottom of the furnace and the loop seal, induced by the agglomeration of particles in these regions. The pressure and pressure gradient decrease gradually along with the bed height. As shown in Fig. 7b, the pressure distributions in three external circulation loops are roughly similar but show large discrepancies in the loop seal region. Specifically, the pressure in the middle loop seal is lower than that in the left and right loop seals by 4.5%. This manifests that fewer particles accumulate in the middle loop seal, and more particles circulate through the left and right loop seals, demonstrating the non-uniform gas–solid distribution in the CFB with multiple cyclones. This non-uniformity calls for the optimization of cyclone arrangements to achieve high CFB performance [38,49].

Fig. 9 shows the time-averaged profiles of solid holdup and pressure gradient along with the bed height. The pressure gradient is found to positively correlate with the solid holdup. The reasons lie in the fact that the pressure gradient is defined by the weight of particles in a specific height interval [50]. The pressure gradient and solid holdup achieve the maximum value in the lower part

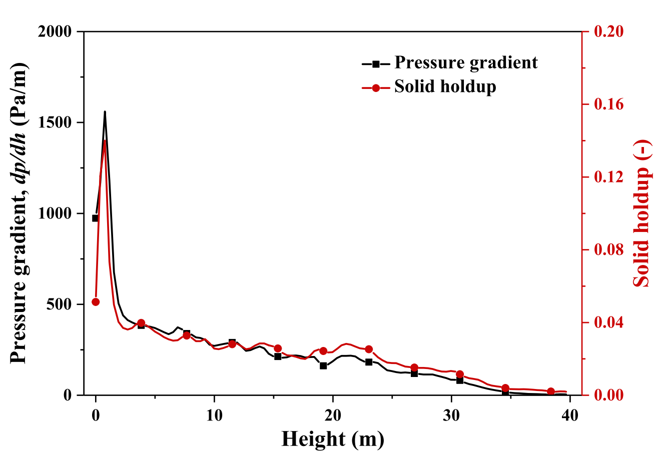

Fig. 9. Profiles of the pressure gradient (dp/dh) and solid holdup in the furnace.

of the furnace due to the combined effects of particle recycling from the loop seal and coal feeding. Above this specific height, the pressure drop and solid holdup decline in the axial direction due to the transition from dense phase to dilute phase.

4.3. Comparison of different coal feeding modes

This section compares the effects of different coal-feeding modes on particle behaviours, gas thermochemical characteristics, and pollutant formation in the 3D full-loop CFB.

4.3.1. Particle behaviours

Particle mixing is a vital indicator to evaluate the transportation intensity of bed material and solid fuels in the CFB, also closely related to the thermochemical performance of the CFB at the particle scale. Specifically, uneven mixing will weaken heat and mass transfer properties (e.g., hot spots in the furnace [12]), reduce combustion efficiency, and further affect overall output. In this study, the Lacey mixing index (MI) [51] is employed to quantitatively assess the particle mixing process, defined as:

$$\mathrm{MI} = \frac{\sigma_0^2 - S^2}{\sigma_0^2 - \sigma_r^2} \tag{33}$$

where σ_0^2 $\left(=\bar{c}\left(1-\bar{c}\right)\right)$ and σ_r^2 $\left(=\bar{c}\left(1-\bar{c}\right)/\bar{n}\right)$ are the variances of total separation and perfect mixing of particles, respectively. S $\left(=\sqrt{\frac{1}{N-1}\sum_{i=1}^{N}\left(\bar{c}-c_i\right)^2}\right)$ denotes the deviation of the current particle mixing state. The mixing index is in the range of 0 to 1, in which MI = 0 represents solid fuels (i.e., coal) and bed material (i.e., sand) are completely segregated while MI = 1 denotes they are fully mixed.

Fig. 10 compares the time-evolution profiles of particle mixing indices between different coal feeding modes. In the start-up stage ($0 \sim 5$ s), the particles initially packed in the lower part of the furnace are fluidized by the introduced airflow. The particles are first entrained to a certain height by the airflow and then fall back under the action of gravity. In this process, the coal particles entering the furnace are entrained by the bed material and gas flow and move upwards. Accordingly, the mixing index first increases and then decreases, and the single-side coal feeding mode has a larger variation magnitude. After 5 s, the mixing indices under the two coal feeding modes increase over time, but the dual-side coal feed-

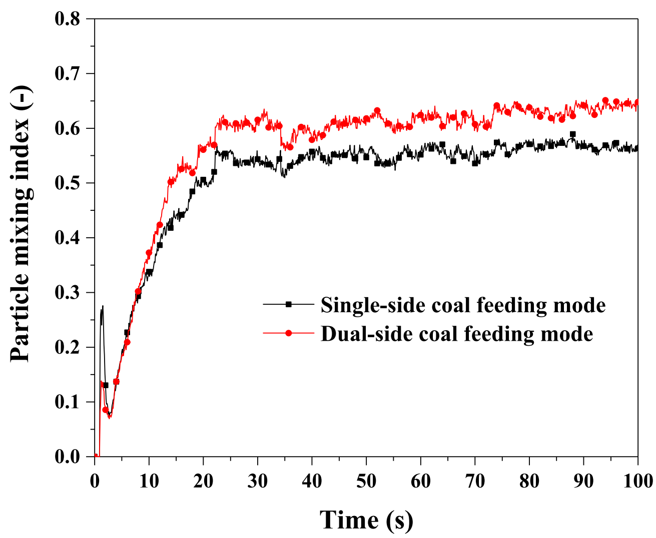

Fig. 10. Comparison of particle mixing indices between different coal feeding modes.

ing mode has a more rapid increase rate than the single-side coal feeding mode. After 40 s, the mixing indices under the two coal feeding modes achieve equilibrium states. The time-averaged mixing indices from 40 s to 100 s are 0.556 and 0.618 for the single-side and dual-side coal feeding modes, respectively, indicating that the dual-side coal feeding mode has a better mixing performance in the furnace.

In addition to the particle mixing, the particle residence time reflects the degree of internal circulation of particles in the CFB furnace [52,53]. Due to the advantage of the present Eulerian-Lagrangian method, the residence time of each particle in the furnace can be obtained by monitoring its trajectory [54]. Fig. 11 shows the residence time distribution (RTD) of coal particles in the furnace under the two coal feeding modes. It is noted that the RTD shows an early peak with an extended tail. The early peak corresponds to those coal particles directly escaping from the furnace while the extended tail corresponds to those coal particles undergoing internal mixing/circulation in the furnace. The RTD of coal particles predicted by the present work is consistent with that from empirical correlations and experimental measurements [52,53,55], further demonstrating the reliability of the present model in simulating complex gas–solid reacting flow in such an industrial-scale CFB.

The time-averaged values of the residence time of coal particles in the furnace are 17.07 s and 18.83 s for the single- and dual-side coal feeding modes, respectively. Table 4 gives the statistics of the residence time of coal particles in the furnace under the two coal feeding modes. As compared with the single-side feeding mode, the residence time of coal particles in the dual-side feeding mode tends to concentrate in the period of 20 s, and the proportion of coal particles with residence time less than 20 s in the furnace is 68.42%, while that in the single-side feeding mode is 72.32%. In contrast, the proportion of residence time over 20 s is 31.58% in the dual-side coal feeding mode, while that in the single-side feeding mode is 27.68%. Due to the higher mixing degree of coal particles in the furnace, coal particles in the furnace with the dual-side coal feeding mode have a longer residence time, leading to more significant heat and mass transfer than that with the single-side coal feeding mode.

Solid flux is a key indicator to characterize the transportation intensity of solid particles in the system, which is defined as a function of solid density, solid velocity, and solid concentration as follows:

$$F_s = \rho_s \cdot U_s \cdot (1 - \theta_g) \quad (34)$$

Fig. 12 shows the time-averaged spatial distribution of the solid flux in the furnace under different coal feeding modes. As shown in Fig. 12 (a) and (b), the furnace with the single-side coal feeding mode shows a strong vertical solid flux (Fsy) near the side walls. Specifically, the positive vertical solid flux appears for the left-side wall due to the gas volume expansion from rapid drying and pyrolysis of coal material while the negative vertical solid flux is observed for the right-side wall because of vigorous solid back mixing. Such an uneven phenomenon is alleviated by the dual-side coal feeding mode, with the vertical solid flux distributed uniformly in the furnace. This tendency can be further indicated by the spatial distributions of horizontal solid flux (Fsx), as shown in Fig. 11 (c) and (d). The magnitude of the horizontal solid flux in the furnace with the single-side coal feeding mode ranges from -600 to 100 kg/(m^2·s), with an average value of 0.7 kg/(m^2·s) and a standard deviation of 37.41 kg/(m^2·s). In contrast, The magnitude of the horizontal solid flux in the furnace with the dual-side coal feeding mode ranges from -100 to 40 kg/(m^2·s), with an average

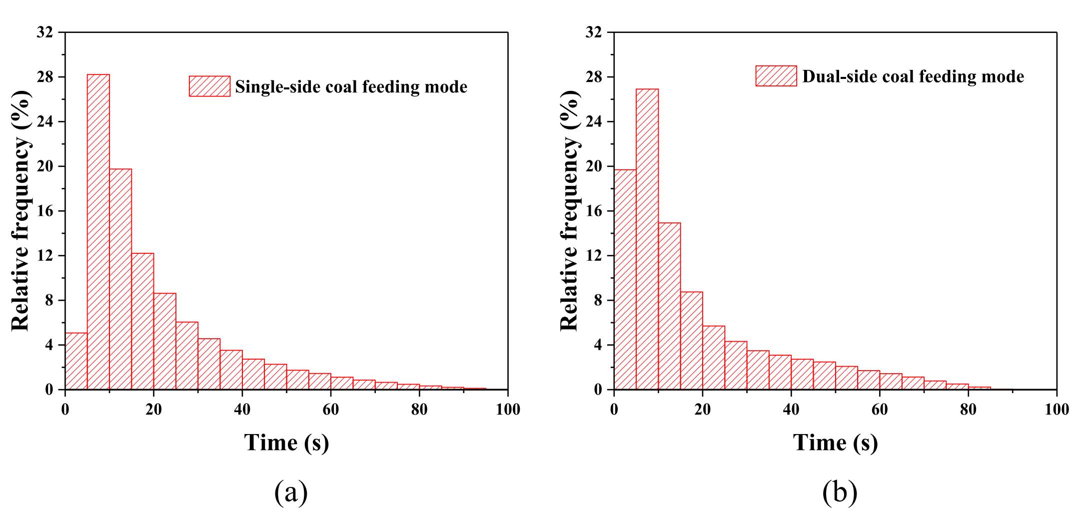

Fig. 11. Residence time distribution (RTD) of coal particles in the furnace under different coal feeding modes: (a) single-side coal feeding mode; (b) dual-side coal feeding mode.

Table 4
Statistics of the residence time of coal particles in the furnace under different coal feeding modes.

The residence time of coal particles (s)	< 20 s	>20 s
Single-side coal feeding mode	72.32%	27.68%
Dual-side coal feeding mode	68.42%	31.58%

value of 0.5 kg/(m^2·s) and a standard deviation of 8.45 kg/(m^2·s). The magnitude and fluctuation (identified by the standard deviation) of the horizontal solid flux are remarkably reduced by the dual-side coal feeding mode, which is expected to inhibit non-uniform temperature distribution and hotspot formation, beneficial to the thermochemical performance of the CFB apparatuses.

4.3.2. Gas physical-thermal-chemical characteristics

As indicated by the previous sections, the coal feeding mode significantly affects bed hydrodynamics in terms of solid mixing, solid residence time, and solid flux. In this section, the role of the coal feeding model in the gas thermochemical characteristics of the CFB is quantified. Fig. 13 compares the time-averaged distribution of gas temperature in the CFB under different coal feeding modes. The significantly non-uniform distribution of gas temperature in the furnace with the single-side coal feeding mode is observed, where the high gas temperature appears near the left wall of the furnace. Under this mode, coal particles concentrate near the left wall, and the secondary air promotes the combustion of coal particles. The high concentration of coal particles and secondary airflow leads to significant exothermic combustion and

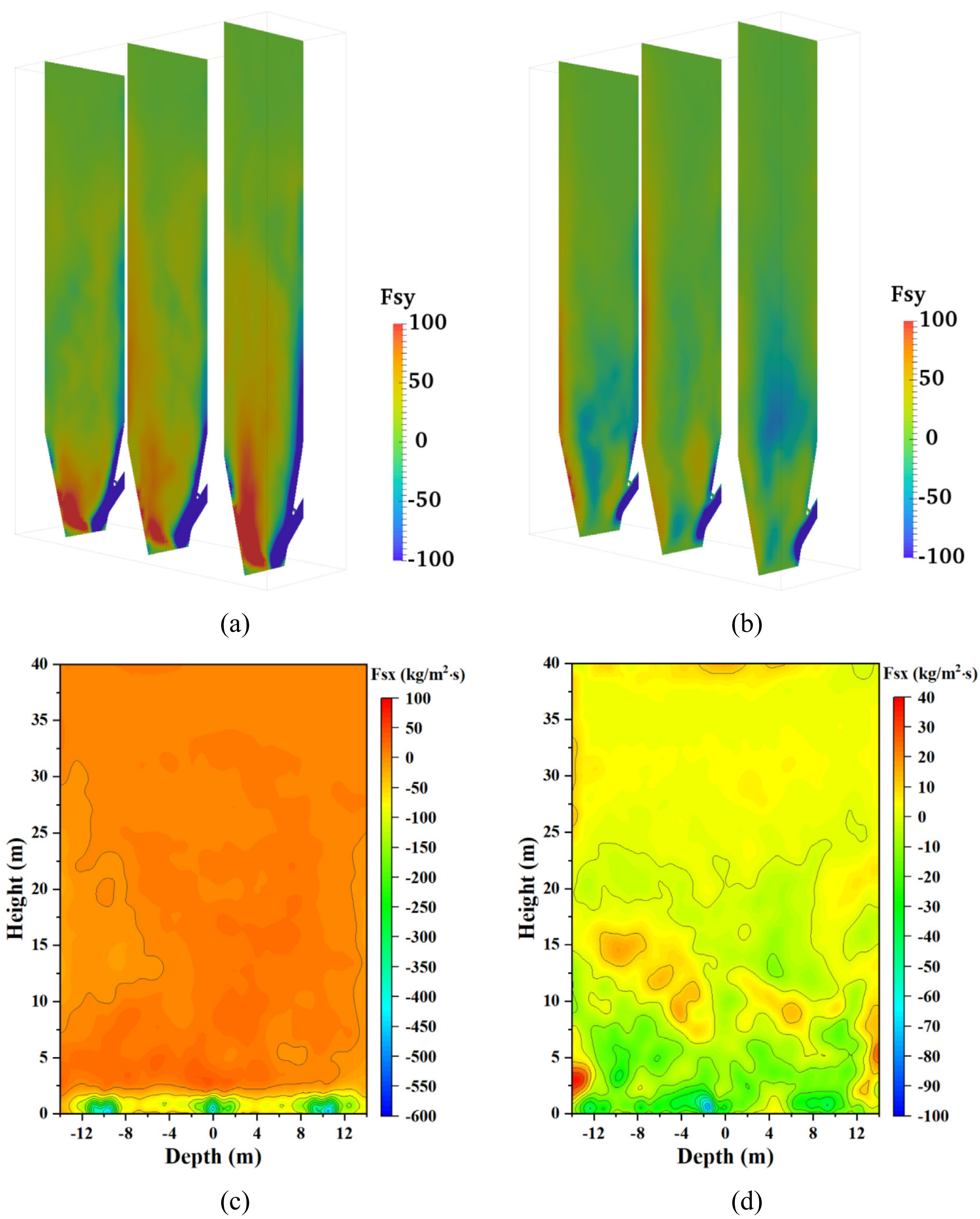

Fig. 12. Spatial distribution of vertical solid flux (Fsy, kg/(m^2·s)) and horizontal solid flux (Fsx, kg/(m^2·s)) in the slice of the CFB under different coal feeding modes: (a) Fsy in the slices z = -10 m, 0 m, and 10 m with the single-side coal feeding mode; (b) Fsy in the slices z = -10 m, 0 m, and 10 m with the single-side coal feeding mode; (c) Fsx in the slice x = 0 m with the single-side coal feeding mode; (d) Fsx in the slice x = 0 m with the dual-side coal feeding mode.

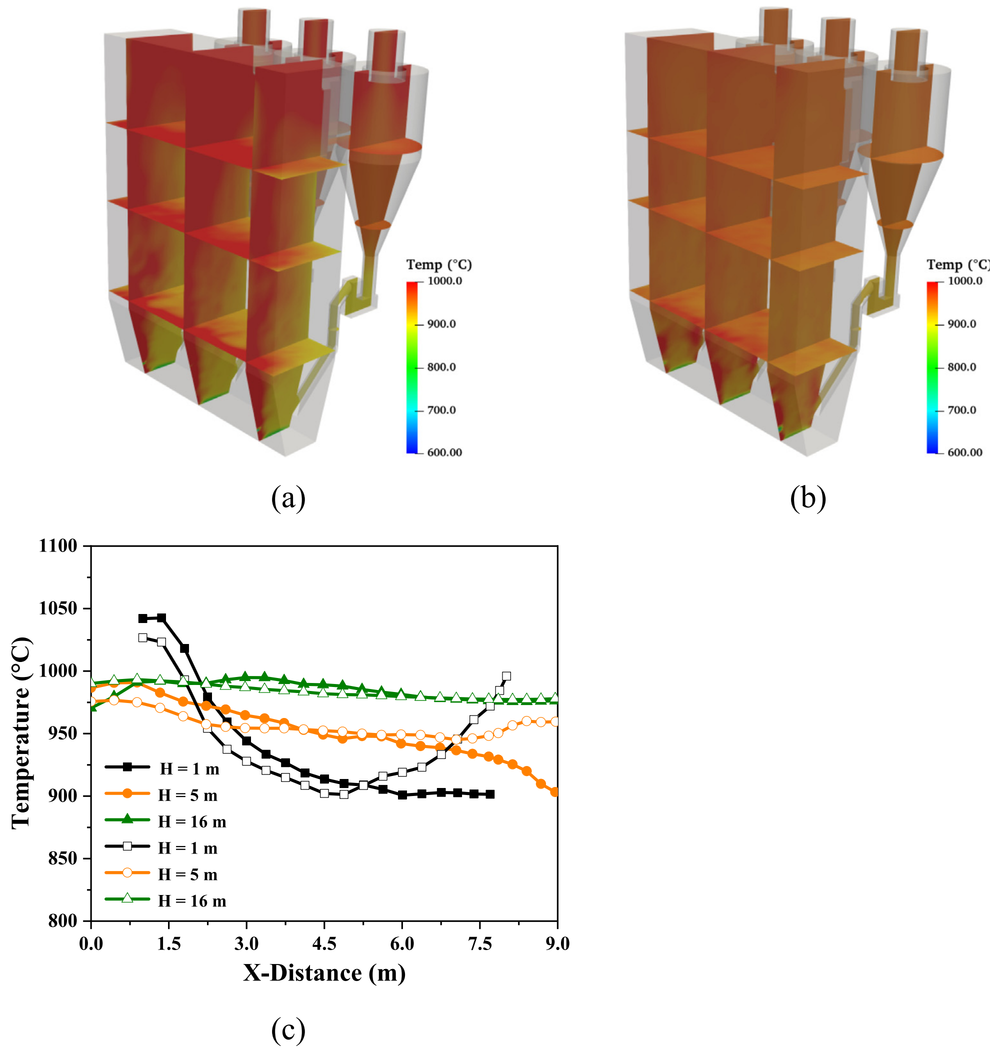

Fig. 13. Comparison of gas temperature in the furnace under different coal feeding modes: (a) contour plot of gas temperature under the single-side coal feeding mode; (b) contour plot of gas temperature under the dual-side coal feeding mode; (c) profiles of gas temperature at different bed heights under different coal feeding modes (solid line: single-side coal feeding model; hollow line: dual-side coal feeding mode).

the resultant uneven temperature distribution near the left wall. Such an uneven temperature distribution leads to some hot spots inside the furnace [56], which will deteriorate the heat and mass transfer characteristics of the CFB. The dual-side coal feeding mode alleviates the uneven temperature distribution, and the magnitude of temperature is similar between the left-side wall and right-side wall. Along with the bed height, a more uniform temperature distribution in the furnace with the dual-side coal feeding mode is observed than that with the single-side coal feeding mode. As shown in Fig. 12(c), the temperature distribution presents the “high on the left and low on the right” at the lower part of the furnace with the single-side coal feeding mode while it shows the “high on both sides and low in the middle” at the lower part of the furnace with the dual-side coal feeding mode. The non-uniformity of the spatial distribution of the temperature gradually weakens with the increased bed height. At the lower part of the furnace, the temperature ranges from 900 °C to 1042 °C with an average value of 938 °C under the single-side coal feeding mode, while it ranges from 902 °C to 1026 °C with an average value of 946 °C under the dual-side coal feeding mode. Therefore, the dual-side coal feeding mode has advantage in providing uniform temperature distribution inside the furnace to the single-side coal feeding mode. The dual-side coal feeding mode enhances the particle mixing performance in the furnace and weakens the aggregation effect of coal particles, further avoiding the generation of hot spots and promoting the stable operation of the CFB.

Fig. 14 and Table 5 further show the qualitative and quantitative statistics of the temperature in the furnace under different coal feeding modes. The temperature distribution within the range of 900 $\sim$ 1000 °C accounts for 97.43% in the dual-side coal feeding mode, while that in the single-side coal feeding mode accounts for 96.38%. In the dual-side coal feeding mode, the low-temperature area (T < 900 °C) and high-temperature area (T > 1000 °C) account for 2.33% and 0.24% respectively, while in the single-side coal feeding mode, they account for 2.46% and 1.16% respectively. Therefore, the CFB with the dual-side coal feeding mode has a narrow temperature distribution than that with the single-side coal feeding mode. Although the proportion of low-temperature area under the two coal feeding modes is similar, there is a higher proportion of high-temperature area in the furnace with the single-side coal feeding mode. Quantitatively, the mean temperature in the furnace with the dual-side coal feeding mode is about 7 °C lower than that with the single-side coal feeding mode, which is known to benefit the alleviation of gas pollutant formation [5,10,57].

Fig. 15 shows the time-averaged distribution of gas species (i.e., CO_2, O_2) in the full-loop CFB under different coal feeding modes. The uneven distribution of coal particles in the furnace with a

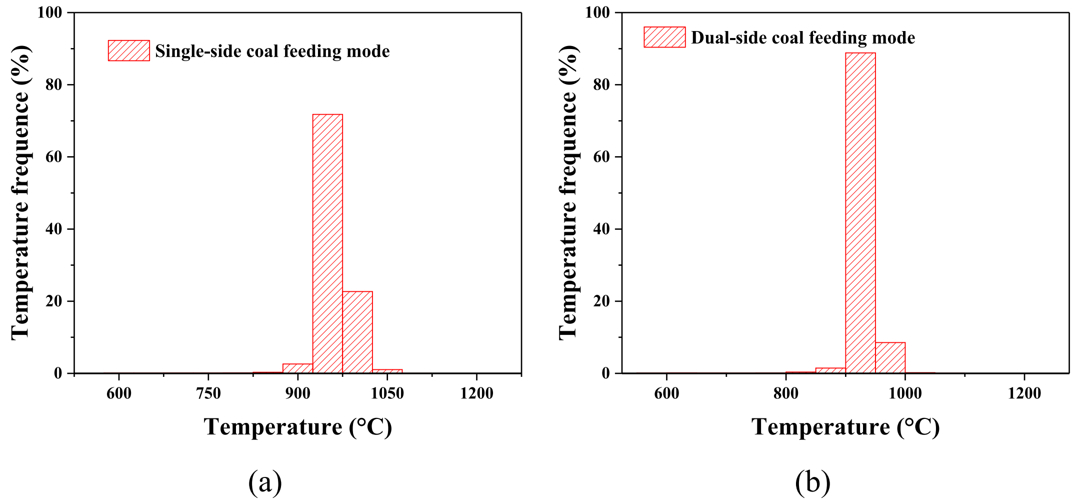

Fig. 14. Histogram distribution of temperature in the CFB under different coal feeding modes: (a) single-side coal feeding mode; (b) dual-side coal feeding mode.

Table 5
Temperature statistics in the CFB.

Temperature (°C)	< 900	900 ~ 1000	> 1000
Single-side coal feeding mode	2.46%	96.38%	1.16%
Dual-side coal feeding mode	2.33%	97.43%	0.24%

single-side coal feeding mode leads to the non-uniform distributions of CO_2 and O_2. Under this mode, the coal particles concentrating near the left wall consume O_2 due to the exothermic oxidation between volatile from coal material and oxygen from airflow. Furthermore, the char residual will also consume oxygen in this region. On the contrary, CO_2 as the main product of oxidation reactions shows the opposite distribution as compared to O_2. A high concentration of O_2 is observed in the loop seal due to the aeration for transporting solid particles from the standpipe into the furnace. CO_2 is nearly zero in the loop-seal because of the close-packing particles in this region. As compared with the single-side coal feeding mode, the coal particles are more evenly distributed in the furnace with the dual-side coal feeding mode, resulting in a more uniform distribution of main gas species (i.e., O_2, CO_2).

Fig. 15 (e) and (f) quantitatively show the distribution of main gas species (i.e., CO_2 and O_2) at different bed heights. Due to the distinct distribution of temperature under these two modes, a similar distribution of gas species can be observed at different bed heights of the furnace. The lower part of the furnace exhibits a large discrepancy between the central region and wall region due to the injection of raw coal material and vigorous oxidation reactions. This discrepancy is smeared out as the bed height increases due to the homogeneous reactions mainly occurring in the upper bed. Specifically, in the single-side coal feeding mode, the concentrations of CO_2 and O_2 at the lower part of the furnace (H = 1 m) are in the range of 0.07 ~ 0.18 and 0.05 ~ 0.16, with average values of 0.114 and 0.124, respectively. In the dual-side coal feeding mode, the concentrations of CO_2 and O_2 at the lower part of the furnace are in the range of 0.13 ~ 0.19 and 0.03 ~ 0.11, with average values of 0.17 and 0.056, respectively. The fluctuation of CO_2 and O_2 concentrations along the X direction under the dual-side coal feeding mode is significantly smaller than that under the single-side coal feeding mode. Moreover, the dual-side coal feeding mode gives rise to a higher mean concentration of CO_2 but a lower mean concentration of O_2 at the lower part of the furnace, indicating that the coal particles are burnt more completely in the corresponding region.

4.3.3. Pollutant formation

The reduction of gas pollutants is one of the main targets to optimize geometry configurations or operating modes to benefit the environment. Fig. 16 regarding the time-averaged contour plots of gas pollutants (e.g., CO, NO, and SO_2) in the full-loop CFB, the gas pollutants under the single-side coal feeding mode are concentrated in the left wall due to the lower O_2 concentration and some species (e.g., NO and SO_2) are filled within the whole furnace. The generated gas pollutants are subsequently released from the cyclone separator, threatening the environment. The dual-side coal feeding mode provides an effective way to reduce gas pollutants by more complete fuel consumption and lower in-furnace temperature. As shown in Fig. 16 (d-f), a lower concentration of gas pollutants can be observed in the whole furnace under the dual-side coal feeding mode.

Fig. 17 quantitatively compares the gas species (i.e., CO_2, O_2, CO, NO, and SO_2) obtained from the CFB outlet after the system archives an equilibrium state under different coal feeding modes. Compared with the single-side coal feeding mode, the dual-side coal feeding gives a higher CO_2 concentration but a lower O_2 concentration, indicating that the coal particles are burnt in the furnace more completely. Moreover, the lower O_2 concentration promotes the formation of CO, which reacts with nitrogen-containing compounds to reduce nitrogen oxide emissions. The lower O_2 concentration also inhibits the oxidation of sulphur-containing and nitrogen-containing compounds. Therefore, the concentrations of SO_2 and NO are reduced by 3% and 5% under the dual-side coal feeding mode than that under the single-side coal feeding mode.

5. Conclusion

In this work, the effect of the coal feeding modes on the hydrodynamics and thermochemical characteristics of a 300 MW_{th} industrial-scale CFB was numerically studied by a recently developed MP-PIC reactive model. The turbulent gas motion was simulated by a large eddy simulation and the particle motion by the discrete particle method, with the particle size distribution, heat transfer, and chemical reactions being fully integrated. The boundary conditions are specified based on the practical measured data. The model is verified by comparing the predicted solid mass flow rate, temperature distribution, and gas species with experimental data, with good agreement realized. The improvement of the in-furnace and external-loop non-uniformity of the CFB by the dual-

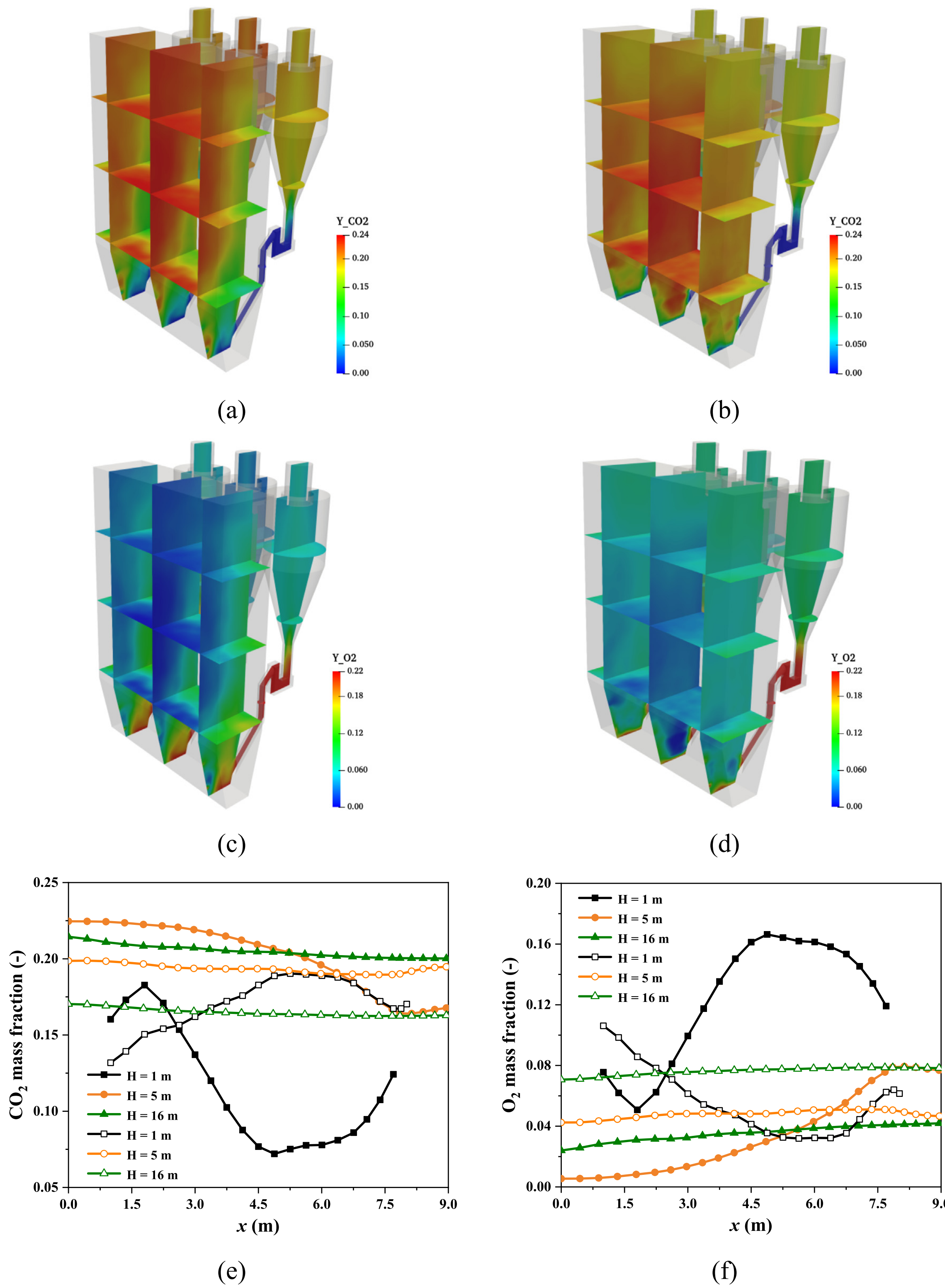

Fig. 15. Comparison of gas species in the furnace under different coal feeding modes: (a) contour plot of CO_2 mass fraction under the single-side coal feeding mode; (b) contour plot of CO_2 mass fraction under the dual-side coal feeding mode; (c) contour plot of O_2 mass fraction under the single-side coal feeding mode; (d) contour plot of O_2 mass fraction under the dual-side coal feeding mode; (e) profiles of CO_2 mass fraction at different bed heights under different coal feeding modes; (f) profiles of O_2 mass fraction at different bed heights under different coal feeding modes (solid line: single-side coal feeding mode; hollow line: dual-side coal feeding mode).

side coal feeding mode is quantified. Under the dual-side coal feeding mode, the spatial distribution inhomogeneity of coal particles and the particle mixing performance are improved, and the magnitude and fluctuation (identified by the standard deviation) of the horizontal solid flux are remarkably reduced. These variations of gas–solid dynamic characteristics under the dual-side coal feeding mode reduce particle segregation induced by density/mass differences, thereby enhancing particle mixing performance and intra-

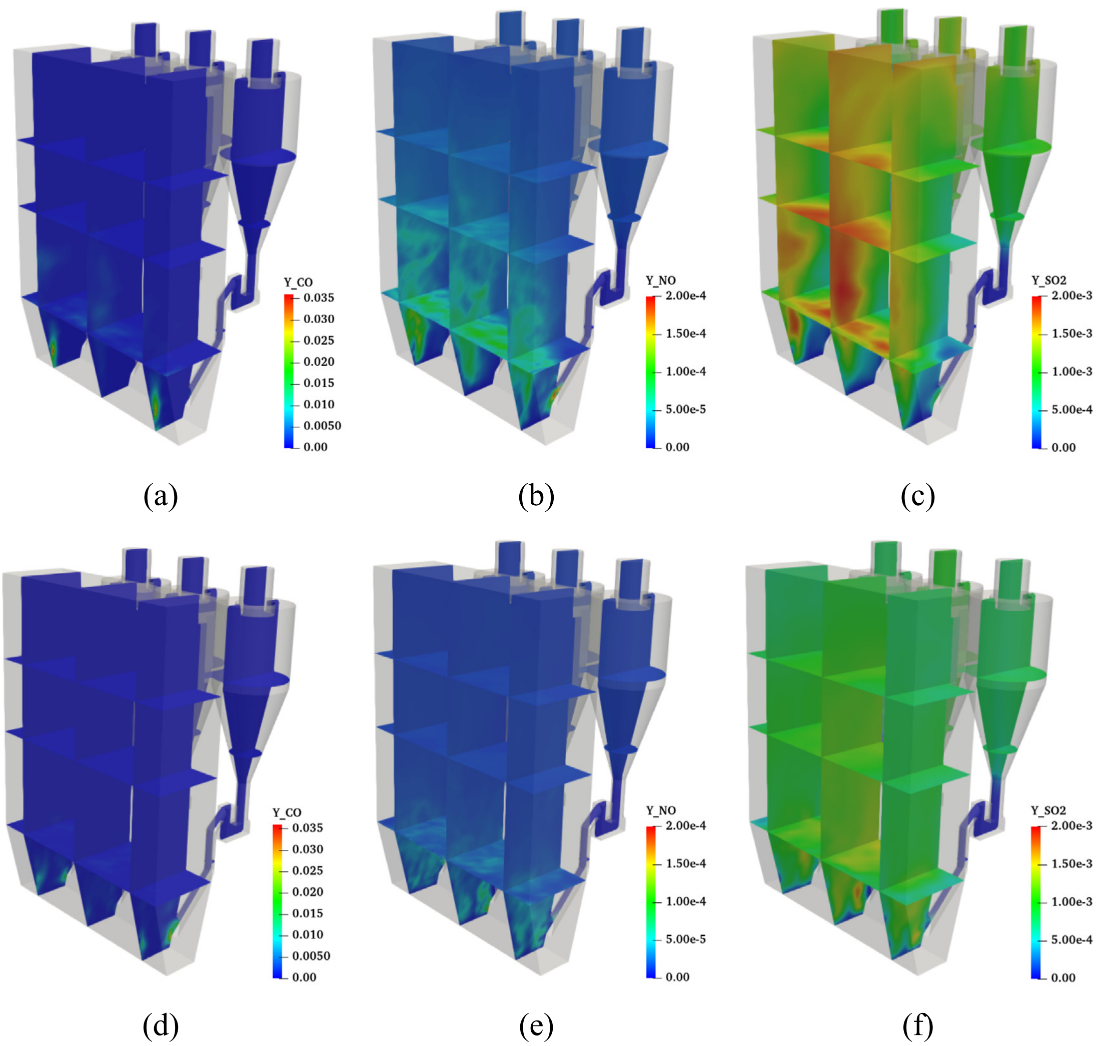

Fig. 16. CO, NO, SO_2 concentration distribution under different coal feeding modes: (a), (b), (c) single-side coal feeding mode; (d), (e), (f) dual-side coal feeding mode.

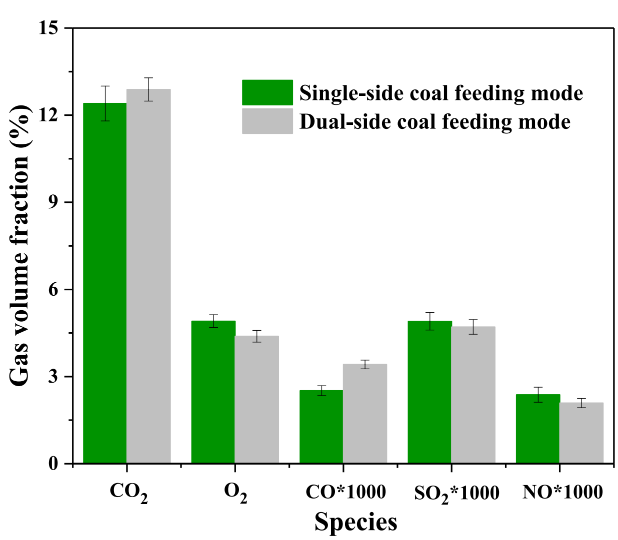

Fig. 17. Comparison of the time-averaged volume fraction of gas pollutants between different coal feeding modes.

phase/inter-phase heat and mass transfer, which is expected to inhibit non-uniform temperature distribution and hotspot formation, beneficial to the pollutants removal and combustion performance of the CFB reactor. The conclusions are as follows:

1) The vertical motion of particles in the furnace is dominant but the horizontal migration of particles is also observed. Large pressure and pressure gradient appear at the bottom of the furnace and the loop seal. The pressure is non-uniformly distributed among three external loops, where the pressure in the middle loop seal is lower than that in the left and right loop seals by 4.5%. The pressure gradient positively correlates with the solid holdup.
2) Under the conditions of a coal feed rate of 44.75 kg/s and an operating temperature of 880 °C, the dual-side coal feeding mode promotes the final mixing degree by 6.7% and extends the residence time of coal particles by 6.9% compared with the single-side coal feeding mode. The RTD of coal particles in the furnace under the two coal feeding modes shows an early peak with an extended tail. The dual-side coal feeding mode significantly reduces the magnitude and fluctuation of the horizontal solid fluxes in the furnace by 28.5% and 77%,

respectively.

3) The CFB with the single-side coal feeding mode shows a significantly non-uniform temperature distribution near the sidewalls. The dual-side coal feeding mode alleviates the uneven temperature distribution in the whole furnace. Specifically, the dual-side coal feeding mode gives a lower proportion of high-temperature area and narrower temperature range in the furnace than the single coal feeding mode. The dual-side coal feeding mode reduces the mean temperature of the furnace by 7 °C.
4) The dual-side coal feeding mode alleviates the uneven distribution of CO_2 and O_2 in the furnace with a single-side coal feeding mode. Besides, the dual-side coal feeding mode gives a higher mean concentration of CO_2 but a lower mean concentration of O_2 at the lower part of the furnace, indicating that the coal particles are burnt more completely. Moreover, the dual-side coal feeding model reduces the concentrations of SO_2 and NO by 3% and 5%, respectively.

In this work, the improvement of flow uniformity and system performance of supercritical CFB using the dual-side coal feeding mode is quantified. The results shed light on the design and operation of low-pollutant and high-efficiency power plants. However, there are some limitations in this work: (i) Insufficient model development. Specifically, the particle is assumed to be spherical, without the non-spherical effect considered. Besides, inter-particle collisions are simplified by a solid stress model, without the fully colliding procedure resolved. Moreover, chemical reactions are described by lumped reaction kinetics, without the intermediate elements considered. More detailed particle properties and reaction kinetics will be considered in our future work. (ii) Lacking economic analysis. The present work mainly focuses on the effects of different coal feeding modes on hydrodynamics and thermochemical behaviors in the CFB. A comprehensive economic analysis, including energy analysis and exergy analysis, is needed in future work. (iii) Narrow operating window. Only limited operating conditions are studied in this work due to the huge computational cost. Artificial intelligence methods such as back propagation neural networks are needed in future work to perform fast predictions based on limited data.

Declaration of Competing Interest

The authors declare that they have no known competing financial interests or personal relationships that could have appeared to influence the work reported in this paper.

Acknowledgment

We are grateful for the support from the National Natural Science Foundation of China (No. 51925603) and the Fundamental Research Funds for the Central Universities (2022ZFJH004).

Appendix A. Supplementary material

Supplementary data to this article can be found online at https://doi.org/10.1016/j.apt.2023.104036.

References

[1] F. Wei, Y. Cheng, Y. Jin, Z. Yu, Axial and lateral dispersion of fine particles in a binary-solid riser, The, Can. J. Chem. Eng. 76 (1998) 19–26.
[2] C. Geng, Y. Shao, W. Zhong, A. Yu, Experiments on particles flow in a dual circulating fluidized bed with symmetrical structure, Powder Technol. 304 (2016) 81–88.
[3] F. Alobaid, J. Peters, R. Amro, B. Epple, Dynamic process simulation for Polish lignite combustion in a 1 MWth circulating fluidized bed during load changes, Appl. Energy 278 (2020).
[4] S. Li, M. Xu, L. Jia, L. Tan, Q. Lu, Influence of operating parameters on N2O emission in O2/CO2 combustion with high oxygen concentration in circulating fluidized bed, Appl. Energy 173 (2016) 197–209.
[5] X. Ke, M. Engblom, H. Yang, A. Brink, J. Lyu, M. Zhang, B. Zhao, Prediction and minimization of NOx emission in a circulating fluidized bed combustor: A comprehensive mathematical model for CFB combustion, Fuel 309 (2022).
[6] T. Li, W.A. Rogers, M. Syamlal, J. Dietiker, J. Musser, M. Shahnam, S. Rabha, The NETL MFiX suite of multiphase flow models: a brief review and recent applications of MFiX-TFM to fossil energy technologies, Chem. Eng. Sci. 169 (2017) 259–272.
[7] J. Chen, W. Yin, S. Wang, G. Yu, J. Li, T. Hu, F. Lin, Modelling of coal/biomass co-gasification in internal circulating fluidized bed using kinetic theory of granular mixture, Energ. Conver. Manage. 148 (2017) 506–516.
[8] J. Lin, K. Luo, S. Wang, L. Sun, J. Fan, Particle-scale study of coal-direct chemical looping combustion (CLC), Energy 250 (2022).
[9] W. Zhou, C.S. Zhao, L.B. Duan, C.R. Qu, X.P. Chen, Two-dimensional computational fluid dynamics simulation of coal combustion in a circulating fluidized bed combustor, Chem. Eng. J. 166 (2011) 306–314.
[10] S. Golshan, R. Sotudeh-Gharebagh, R. Zarghami, N. Mostoufi, B. Blais, J. Kuipers, Review and implementation of CFD-DEM applied to chemical process systems, Chem. Eng. Sci. 221 (2020).
[11] J. Azmir, Q. Hou, A. Yu, CFD-DEM study of the effects of food grain properties on drying and shrinkage in a fluidised bed, Powder Technol. 360 (2020) 33–42.
[12] C. Hu, K. Luo, M. Zhou, J. Lin, D. Kong, J. Fan, Influences of secondary gas injection pattern on fluidized bed combustion process: A CFD-DEM study, Fuel 268 (2020).
[13] S. Wang, K. Luo, J. Fan, CFD-DEM coupled with thermochemical sub-models for biomass gasification: Validation and sensitivity analysis, Chem. Eng. Sci. 217 (2020).
[14] J. Lin, L. Sun, K. Luo, D. Kong, J. Fan, Three-dimensional simulation of a gas-fueled chemical looping combustion system with dual circulating fluidized bed reactors, Energy 246 (2022).
[15] S. Wang, Y. Shen, Particle-scale modelling of the pyrolysis of end-of-life solar panel particles in fluidized bed reactors, Resour. Conserv. Recycl. 183 (2022).
[16] M. Zeneli, A. Nikolopoulos, N. Nikolopoulos, P. Grammelis, S. Karellas, E. Kakaras, Simulation of the reacting flow within a pilot scale calciner by means of a three phase TFM model, Fuel Process. Technol. 162 (2017) 105–125.
[17] D. Kong, S. Wang, M. Zhou, K. Luo, C. Hu, D. Li, J. Fan, Three-dimensional full-loop numerical simulation of co-combustion of coal and refuse derived fuel in a pilot-scale circulating fluidized bed boiler, Chem. Eng. Sci. 220 (2020).
[18] J. Gu, Y. Shao, W. Zhong, Study on oxy-fuel combustion behaviors in a S-CO2 CFB by 3D CFD simulation, Chem. Eng. Sci. 211 (2020).
[19] P.J. Blaser, G. Corina, Validation and application of computational modeling to reduce erosion in a circulating fluidized bed boiler, Int. J. Chem. React. Eng. 10 (2012).
[20] J. Xie, W. Zhong, Y. Shao, Q. Liu, L. Liu, G. Liu, Simulation of combustion of municipal solid waste and coal in an industrial-scale circulating fluidized bed boiler, Energy Fuel 31 (2017) 14248–14261.
[21] D.M. Snider, S.M. Clark, P.J. O'Rourke, Eulerian-Lagrangian method for three-dimensional thermal reacting flow with application to coal gasifiers, Chem. Eng. Sci. 66 (2011) 1285–1295.
[22] P.J.O. Rourke, D.M. Snider, An improved collision damping time for MP-PIC calculations of dense particle flows with applications to polydisperse sedimenting beds and colliding particle jets, Chem. Eng. Sci. 65 (2010) 6014–6028.
[23] J. Smagorinsky, General circulation experiments with the primitive equations: I, The basic experiment, Monthly weather review. 91 (1963) 99–164.
[24] P.J.O. Rourke, P.P. Zhao, D. Snider, A model for collisional exchange in gas/liquid/solid fluidized beds, Chem. Eng. Sci. 64 (2009) 1784–1797.
[25] J. Xie, W. Zhong, A. Yu, MP-PIC modeling of CFB risers with homogeneous and heterogeneous drag models, Adv. Powder Technol. 29 (2018) 2859–2871.
[26] Z. Wan, S. Yang, Y. Sun, Y. Wei, J. Hu, H. Wang, Distribution and particle-scale thermochemical property of biomass in the gasifier of a dual fluidized bed, Energ. Conver. Manage. 209 (2020).
[27] S. Kraft, F. Kirnbauer, H. Hofbauer, CPFD simulations of an industrial-sized dual fluidized bed steam gasification system of biomass with 8MW fuel input, Appl. Energy 190 (2017) 408–420.
[28] S.E. Harris, D.G. Crighton, Solitons, solitary waves, and voidage disturbances in gas-fluidized beds, J. Fluid Mech. 266 (1994) 243–276.
[29] R. Beetstra, M.A. van der Hoef, J.A.M. Kuipers, Numerical study of segregation using a new drag force correlation for polydisperse systems derived from lattice-Boltzmann simulations, Chem. Eng. Sci. 62 (2007) 246–255.
[30] R. Beetstra, M.A. van der Hoef, J. Kuipers, Drag force of intermediate Reynolds number flow past mono-and bidisperse arrays of spheres, AIChE J 53 (2007) 489–501.
[31] A. Gungor, N. Eskin, Two-dimensional coal combustion modeling of CFB, Int. J. Therm. Sci. 47 (2008) 157–174.
[32] H. Yoon, J. Wei, M.M. Denn, A model for moving-bed coal gasification reactors, AIChE J 24 (1978) 885–903.
[33] R. Loison, Pyrolyse rapide du charbon, 1964.
[34] Y. Wu, D. Liu, L. Duan, J. Ma, J. Xiong, X. Chen, Three-dimensional CFD simulation of oxy-fuel combustion in a circulating fluidized bed with warm flue gas recycle, Fuel 216 (2018) 596–611.
[35] X. Ku, T. Li, T. Løvås, CFD–DEM simulation of biomass gasification with steam in a fluidized bed reactor, Chem. Eng. Sci. 122 (2015) 270–283.
[36] S. Wang, Y. Shen, Particle-scale study of heat and mass transfer in a bubbling fluidised bed, Chem. Eng. Sci. 240 (2021).

[37] D.B. Li, C.F. Sun, Y.X. Feng, Numerical simulation research on gas-solid flow and combustion process of 300 MW circulated fluidized bed and related engineering applications, Guangdong Electric, Power 31 (2018) 56–65.
[38] S. Wang, K. Luo, C. Hu, J. Fan, CFD-DEM study of the effect of cyclone arrangements on the gas-solid flow dynamics in the full-loop circulating fluidized bed, Chem. Eng. Sci. 172 (2017) 199–215.
[39] B. Lu, N. Zhang, W. Wang, J. Li, J.H. Chiu, S.G. Kang, 3-D full-loop simulation of an industrial-scale circulating fluidized-bed boiler, AIChE J 59 (2013) 1108–1117.
[40] J. Bai, C. Yu, L. Li, X. Li, Q. Wang, Z. Luo, Experimental investigation on co-firing of coal and refuse-derived fuel in a pilot-scale circulating fluidized bed combustor, Zhongguo Dianji Gongcheng Xuebao(Proceedings of the Chinese Society of Electrical Engineering), Chinese Society for, Electr. Eng. (2012) 36–41.
[41] J. Bruchmüller, B. Van Wachem, S. Gu, K.H. Luo, R.C. Brown, Modeling the thermochemical degradation of biomass inside a fast pyrolysis fluidized bed reactor, AIChE J 58 (2012) 3030–3042.
[42] C. Hu, K. Luo, S. Wang, L. Sun, J. Fan, Computational fluid dynamics/discrete element method investigation on the biomass fast pyrolysis: The influences of shrinkage patterns and operating parameters, Ind. Eng. Chem. Res. 58 (2018) 1404–1416.
[43] A.N. Hayhurst, M.S. Parmar, Does solid carbon burn in oxygen to give the gaseous intermediate CO or produce CO2 directly?, Some experiments in a hot bed of sand fluidized by air, Chemical Engineering Science 53 (1998) 427–438.
[44] A.N. Hayhurst, M.S. Parmar, Measurement of the mass transfer coefficient and Sherwood number for carbon spheres burning in a bubbling fluidized bed, Combust. Flame 130 (2002) 361–375.
[45] Y. Geng, D. Che, An extended DEM–CFD model for char combustion in a bubbling fluidized bed combustor of inert sand, Chem. Eng. Sci. 66 (2011) 207–219.
[46] S. Yang, S. Wang, H. Wang, Numerical study of biomass gasification in a 0.3 MWth full-loop circulating fluidized bed gasifier, Energ. Conver. Manage. 223 (2020).
[47] J.J. Derksen, H. Van den Akker, S. Sundaresan, Two-way coupled large-eddy simulations of the gas-solid flow in cyclone separators, AIChE J 54 (2008) 872–885.
[48] S. Wang, K. Luo, C. Hu, J. Fan, Particle-scale investigation of heat transfer and erosion characteristics in a three-dimensional circulating fluidized bed, Ind. Eng. Chem. Res. 57 (2018) 6774–6789.
[49] X. Zhou, L. Cheng, Q. Wang, Z. Luo, K. Cen, Non-uniform distribution of gas–solid flow through six parallel cyclones in a CFB system: An experimental study, Particuology. 10 (2012) 170–175.
[50] S. Ergun, A.A. Orning, Fluid flow through randomly packed columns and fluidized beds, Ind. Eng. Chem. 41 (1949) 1179–1184.
[51] P.M.C. Lacey, Developments in the theory of particle mixing, J. Appl. Chem. 4 (1954) 257–268.
[52] R. Andreux, G. Petit, M. Hemati, O. Simonin, Hydrodynamic and solid residence time distribution in a circulating fluidized bed: experimental and 3D computational study, Chem. Eng. Process. 47 (2008) 463–473.
[53] L. Hua, J. Wang, Residence time distribution of particles in circulating fluidized bed risers, Chem. Eng. Sci. 186 (2018) 168–190.
[54] S. Wang, K. Luo, C. Hu, L. Sun, J. Fan, Effect of superficial gas velocity on solid behaviors in a full-loop CFB, Powder Technol. 333 (2018) 91–105.
[55] A.T. Harris, J.F. Davidson, R.B. Thorpe, Particle residence time distributions in circulating fluidised beds, Chem. Eng. Sci. 58 (2003) 2181–2202.
[56] C. Hu, K. Luo, S. Wang, L. Sun, J. Fan, Influences of operating parameters on the fluidized bed coal gasification process: A coarse-grained CFD-DEM study, Chem. Eng. Sci. 195 (2019) 693–706.
[57] A. Zhou, H. Xu, M. Xu, W. Yu, Z. Li, W. Yang, Numerical investigation of biomass co-combustion with methane for NOx reduction, Energy 194 (2020).